공학박사학위논문

On the mechanism of RMP-driven pedestal transport and ELM suppression in KSTAR

KSTAR의 공명 자장 섭동이 구동하는 페데스탈 수송 및 경계 불안정성 억제 기작 연구

2020 년 8 월

서울대학교 대학원

에너지시스템공학부

김 상 균

공학박사학위논문

On the mechanism of RMP-driven pedestal transport and ELM suppression in KSTAR

KSTAR의 공명 자장 섭동이 구동하는 페데스탈 수송 및 경계 불안정성 억제 기작 연구

2020 년 8 월

서울대학교 대학원

에너지시스템공학부

김 상 균

On the mechanism of RMP-driven pedestal transport and ELM suppression in KSTAR

KSTAR의 공명 자장 섭동이 구동하는 페데스탈 수송 및 경계 불안정성 억제 기작 연구

지도교수 나 용 수

이 논문을 공학박사 학위논문으로 제출함

2020 년 5 월

서울대학교 대학원

에너지시스템공학부 원자핵공학전공

김 상 균

김 상 균의 공학박사 학위논문을 인준함

2020 년 7 월

위 원 장	황용석	(인)
부위원장	나용수	(인)
위 원	함택수	(인)
위 원	권오진	(인)
위 원	인용균	(인)

Abstract

Sang Kyeun Kim
Department of Energy Systems Engineering
The Graduate School
Seoul National University

A tokamak is a torus device that uses a helical magnetic field to confine a hot plasma. It has been developed to produce controlled thermonuclear fusion power. For the ignition of fusion, high-performance plasma must be sustained for sufficient time. Plasma instability can cause a strong perturbation in the plasma and worsen the plasma confinement. Therefore, it is essential to understand and control the plasma instability.

Edge Localized Modes (ELM) are rapid Magneto-hydrodynamics (MHD) events occurring at the edge region of tokamak plasmas, which can result in damages to the divertor plates. Various methods were developed to control ELM, and among them, the ELM suppression by resonant magnetic perturbation (RMP) showed promising results. Therefore, to fully suppress ELMs via RMP is of great interest to reach and sustain high-performance H-mode discharges. It was found that certain conditions must be met for the RMP-driven ELM crash suppression, so understanding its mechanism is crucial for reliable ELM control using RMP.

This thesis addresses the effect of RMP on pedestal transport and the mechanism of RMP-driven ELM suppression. They are investigated with nonlinear reduced MHD simulations on KSTAR plasmas. First, I developed a numerical method to reconstruct accurate plasma equilibrium, which is an essential component for these state-of-the-art simulations. I employed theoretical models and numerical schemes to solve obstacles in kinetic equilibrium reconstruction. Second, the effect of RMP on pedestal transport is investigated. The numerical simulation shows that RMP forms the kink-peeling structure, the stochastic layer, and neoclassical toroidal viscosity (NTV). The convective and conductive radial fluxes from these responses increase the radial transport and result in the degradation of the pedestal.

Finally, I successfully reproduce ELM suppression by RMP in agreement with experiments. One of the main conclusion of this work is that the ELM crash suppression is attributable not only to the degraded pedestal but also to direct a coupling between ELM and RMP-driven plasma response. The coupling effect 1) enhances the size of magnetic islands at the pedestal, reducing the instability source by further pedestal degradation, and 2) increases the spectral transfer between edge harmonics preventing catastrophic growth and crash of the most unstable modes. Due to these effects, ELMs are non-linearly saturated, and the peeling-ballooning mode activity persists during the suppression phase without a sharp mode crash. I discuss a condition to reinforce this coupling effect for ELM suppression.

In summary, this thesis reveals the importance of plasma response and mode coupling to explain the RMP-driven pedestal transport and ELM suppression. In particular, it improves the previous understanding of the mechanism by discovering the contribution of nonlinear mode interaction on the ELM suppression

mechanism. Based on this study, new insight and approach for ELM control are expected to be developed.

Keywords: Tokamak, 3D field, Edge pedestal, ELM suppression, KSTAR, PBM, Nonlinear MHD

Student Number: 2014-22715

Contents

List of Figures

Chapter 1

Introduction

Energy is a fundamental component of human life. It is the key to human society for every activity and problem. As civilization develops, energy demand increases drastically. Therefore, sustainable and clean energy resources will become more and more critical in the future. There are various energy sources that humans can extract from the Earth. Among the various energy sources, nuclear fusion has a strong potential to be a future energy source. It uses abundant hydrogen as fuel and is an eco-friendly source.

Nuclear fusion is the process by which more than one nuclei combine to form a single nucleus. In this process, energy is released because the mass outcome is smaller than the income, following Einstein's mass-energy conservation law, $E = mc^2$. The goal of present studies on the controlled nuclear fusion is to produce energy from the fusion reaction between two hydrogen isotopes; Deuterium (D) and Tritium (T). This reaction can be expressed as

$$ {}^{2}_{1}D + {}^{3}_{1}T \rightarrow {}^{4}_{2}He\,(3.5\ \text{MeV}) + {}^{1}_{0}He\,(14.1\ \text{MeV})\,. \tag{1.1} $$

D-T reaction is one of the fusion processes which requires the smallest income energy. Therefore, it is most easily accessible, and this is why present research is focused on it. Since the energy outcome of this reaction (17.6 MeV) is much higher than income energy to overcome the coulomb barrier (0.01 MeV), the D-T reaction is a promising way to generate energy and electricity in future fusion power plant. It takes a temperature of over 100 million K to start a D-T reaction without a massive gravity like the sun. At this high temperature, the hydrogen is fully ionized and becomes plasma, the fourth state of matter. However, it is not trivial to sustain high energy particles, and confinement of hot plasma for nuclear fusion is very challenging.

1.1 Tokamak

For the fusion reaction, it is essential to sustain the hot and dense plasma in a limited space. Furthermore, high energy is required to increase the plasma temperature with limited heating sources and maintain a long time operation. One effective way is Magnetic Confinement. Since plasma is a charged particle, it is possible to confine the plasma with a magnetic field configuration. A tokamak is one of the promising thermonuclear fusion devices based on this concept. Unlike other linear magnetic confinement devices, particles cannot escape at each end in the tokamak. The tokamak is designed to prevent the particle loss at the ends by bending the linear device into a torus, making a helical magnetic field configuration. Its structure can be found in Fig.1.1.

A tokamak was firstly invented by Igor Tamm and Andrei Sakharov in the 1950s. Through decades, the concept and physics of tokamak were developed

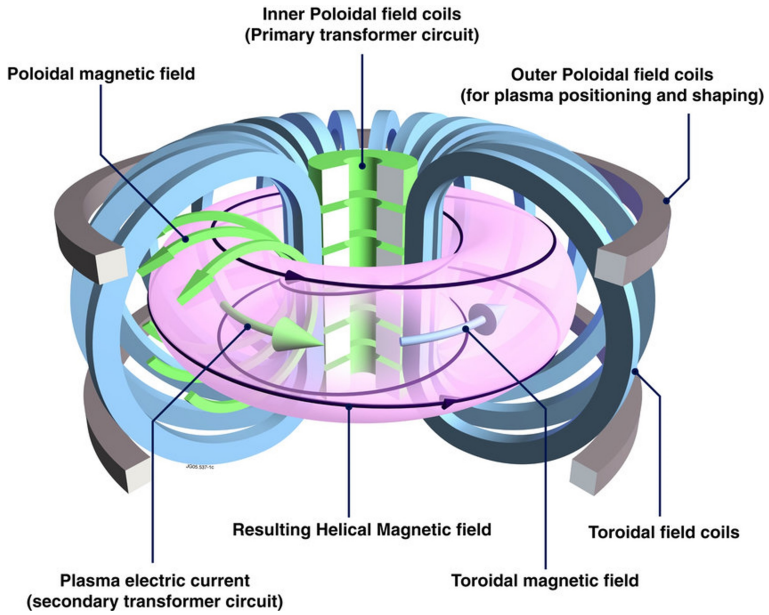

Figure 1.1: Schematic view of the tokamak with plasma current and helical magnetic field [1].

within multiple devices, including TFTR (USA), DIII-D (USA), JET (Europe), JT-60U (Japan), and KSTAR (Korea). These experiments show a possibility of the tokamak as a power plant by reaching high plasma performance. For investigating its practical potential, International Thermonuclear Experimental Reactor, ITER, is under reconstruction in France, which is the outcome of extensive international collaboration.

Despite being the most promising device, the tokamak is still facing problems such as MHD instabilities. These instabilities induce large heat damage to the plasma-facing components and degrade the plasma performance. Therefore, they should be controlled and suppressed to sustain high confinement performance for future fusion devices, including ITER, which is key for the realization of nuclear fusion.

The high confinement plasma operation mode (H-mode) is one of the candidates for fusion plasma operations in ITER. The H-mode plasma is characterized by having an edge transport barrier. The edge transport barrier is generally understood to occur when the $E \times B$ shearing rate, which stabilizes turbulence [8, 9], exceeds a critical threshold in the edge region. As a result of the edge transport barrier, a pedestal is formed at the edge, leading to an overall increase in plasma confinement through profile stiffness [10].

1.2 Edge localized mode

However, the high-pressure gradient in the pedestal and subsequent high edge bootstrap current density can cause so-called Edge Localized Modes (ELM). Peeling-ballooning modes (PBM) [4,11], driven by current density (peeling) and pressure gradient (ballooning), are considered the dominant MHD instability resulting in ELM. The structure of a typical ELM can be found in 1.2(a).

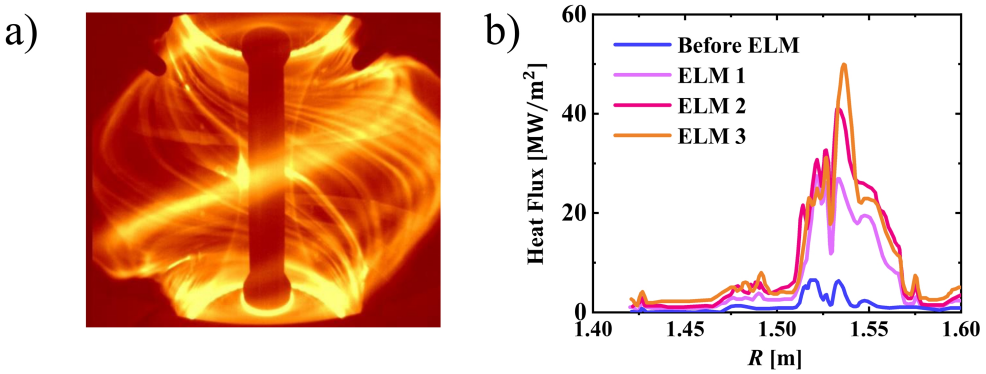

Figure 1.2: Experimental observation of (a) Edge localised mode (ELM) [2] and (b) the transient ELM heat flux on divertor [3].

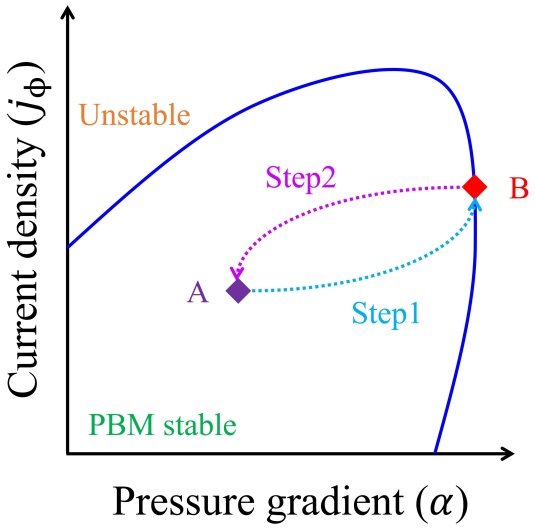

Figure 1.3: Schematic diagram for a ELM cycle [4]

An ELM cycle can be sketched in Fig.1.3. The figure shows the change of the maximum pressure gradient (α) and current density (j_ϕ) of the pedestal. Here, the blue line corresponds to the marginal PBM stability limit. In the beginning, a pedestal starts from low α and j_ϕ values (point A). When pedestal grows due to external heating, α increases, and j_ϕ also increases as the edge bootstrap current increases [12] (step1). The pedestal can grow until it reaches the stability boundary (point B). When pedestal exceeds the stability limit, PBM becomes unstable, leading to the collapse of the edge pedestal (step2). During the pedestal collapse, hot and dense particles are expelled from the main plasma. In the end, the pedestal returns to the initial point, and the next ELM cycle begins.

ELM induces the periodic collapse of the pedestal and releases transient heat fluxes to the plasma-facing components, which can result in significant heat loads on the divertor targets, as shown in Fig.1.2(b). In future devices such as ITER and DEMO, divertor heat fluxes during ELMs are expected to exceed the order of a few $\mathrm{GW/m^2}$ [13,14], which can cause severe damage to plasma-facing materials. Therefore, a reliable way to control or suppress ELMs is essential for the high-performance steady-state operation based on the H-mode regime. In previous studies, pellet injection [15], edge impurity seeding [16], and vertical kick [17] have been found to be effective in mitigating ELMs. Their principle was making PBM more unstable and transforming giant ELMs into smaller frequent ELMs. Nevertheless, in large devices such as ITER, even small ELMs can be dangerous, so full ELM suppression must be achieved.

1.3 RMP-driven ELM suppression

It is widely known that the presence of small non-axisymmetric field perturbation can change the plasma stability. In particular, resonant magnetic field perturbations (RMPs), whose pitch angle is well aligned with the plasma equilibrium field, have a substantial effect on the plasma [18]. RMPs using external magnetic coils are one of the effective ways of suppressing ELMs. It has been found that RMPs can fully suppress ELMs in DIII-D [19], KSTAR [6], EAST [20], and ASDEX Upgrade [21]. Also, RMP is the promising ELM control method in ITER [22]. However, experimental results show that certain conditions must be satisfied for the RMP-driven ELM crash suppression, and the operation window is very narrow [23]. Therefore, understanding its mechanism is crucial to obtain a reliable ELM method using RMP.

The 'initial understanding' (or 'hypothesis') of RMP-driven ELM suppression can be expressed in Fig.1.4. When 1) RMPs of toroidal mode "n" are applied, the field perturbations 2) penetrate into the plasma and induce magnetic islands at the rational surfaces with $q = m/n$, where m and n denote the poloidal and toroidal mode numbers, respectively. Because the rational surfaces are sufficiently dense at the plasma edge, the islands can overlap each other to 3) form a stochastic layer and increase radial transport. Increased radial transport in the stochastic layer can occur due to parallel transport across the stochastic fields, described by the Braginskii model. As a result, the ELM is suppressed as the pedestal slope 4) remains below the marginal stability limit. However, this picture has certain limitations in explaining the experimental observation in KSTAR where coherent PBM-like mode structures with n different from that of RMPs remain during the ELM suppression phase [24]. In addition, the bifurcation of mode rotation in the edge region was found to be closely related to

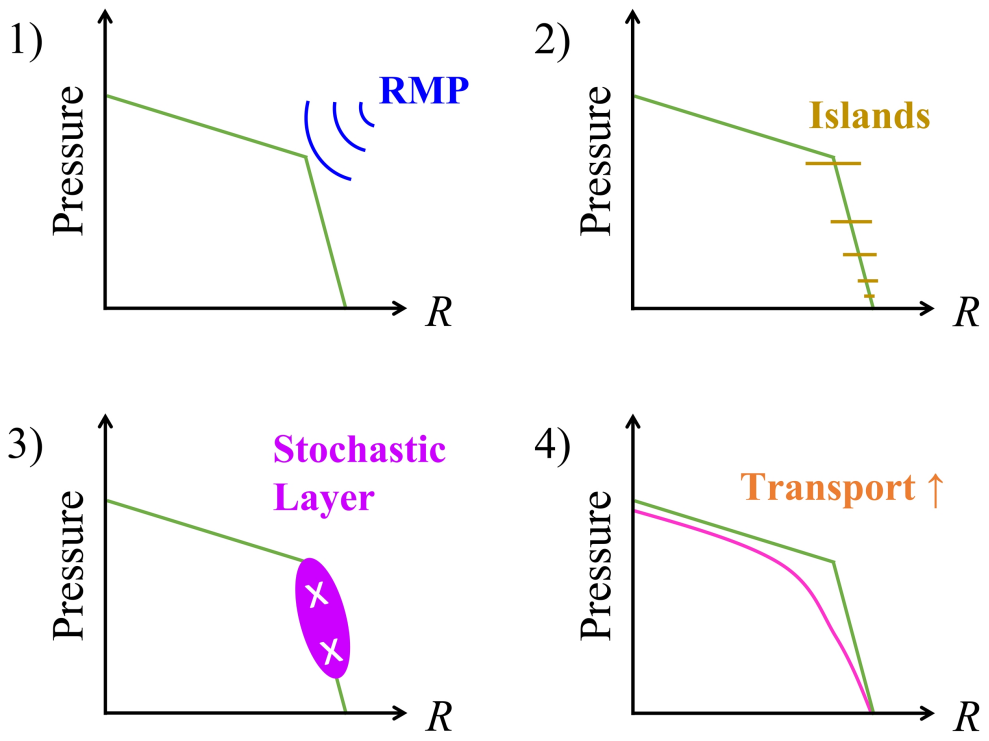

Figure 1.4: Schematic diagrams for the initial understanding of RMP-driven ELM suppression mechanism

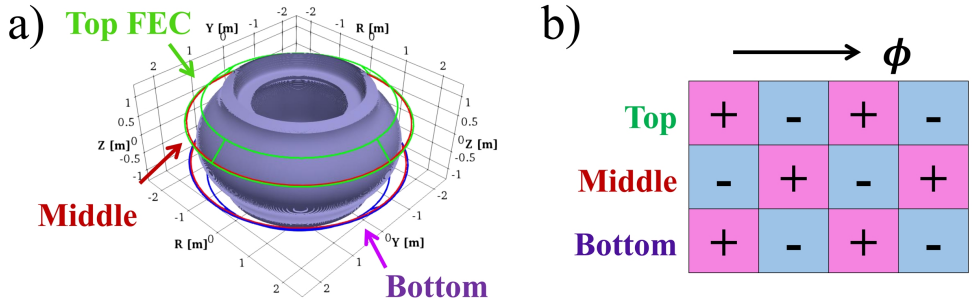

Figure 1.5: (a) KSTAR IVCC coil structure in 3D [5], (b) the RMP coil configuration in the reference equilibrium with three poloidal FEC coils [6]

mode suppression [25]. Therefore, the initial understanding may have difficulties in explaining these experimental findings, and it indicates that additional physics properties should be included to understand the mechanism.

1.4 Objectives and outline of this dissertation

The presence of RMPs can change the radial pedestal transport and the characteristic of ELM. Their mechanisms are investigated in this dissertation using nonlinear reduced MHD simulations in KSTAR equipped with the 3D coils shown in Fig.1.5. KSTAR is a super-conducting tokamak with various plasma diagnostics. Based on its flexible RMP system, KSTAR is in a unique position for robust RMP ELM suppression experiment, so it is advantageous for RMP study with nonlinear MHD simulations.

Chapter 2 describes the strategy to reconstruct an accurate equilibrium in KSTAR, which is essential for advanced delicate simulations. A numerical tool is developed to reconstruct an accurate numerical equilibrium in KSTAR experiments. Various theoretical and numerical schemes to solve the obstacles in equilibrium calculation are introduced.

Chapter 3 presents the analysis of pedestal transport under the presence of RMP. The simulated effect of kink-peeling response and stochastic layer, which is driven by RMP, to the pedestal transport is quantitatively validated with the experimental measurement.

Chapter 4 shows the numerical reproduction of RMP-driven ELM suppression. It has been found that ELM crash suppression is attributable not only to the degraded pedestal but also to a direct coupling between the ELM and the RMP-driven plasma response. Detailed analysis of the role of coupling effects and favorable condition to mode coupling are discussed.

Finally, Chapter 5 summarizes contents and suggests future work.

Chapter 2

Development of advanced equilibrium tool in KSTAR

An accurate numerical plasma equilibrium is essential for plasma physics analysis. Especially, numerically sensitive codes such as nonlinear MHD codes require delicate equilibria. Several codes have been developed to calculate the equilibrium of the experimental plasma. Among them, the EFIT code [26] showed good performance and is widely used as a standard tool in various devices, including DIII-D, JET, and KSTAR.

In EFIT calculations, various experimental measurements and numerical constraints are used. In particular, plasma diagnostics, including magnetic flux near the plasma wall, the field pitch angle, and the pressure profile from kinetic profile measurements, are key components. Here, the Motional Stark effect (MSE) [27] diagnostic is generally used to measure the pitch angle. The equilibrium created only with flux information is defined as MAG-EFIT. When MSE is included, or all three are included, it is called MSE-EFIT or kinetic-EFIT,

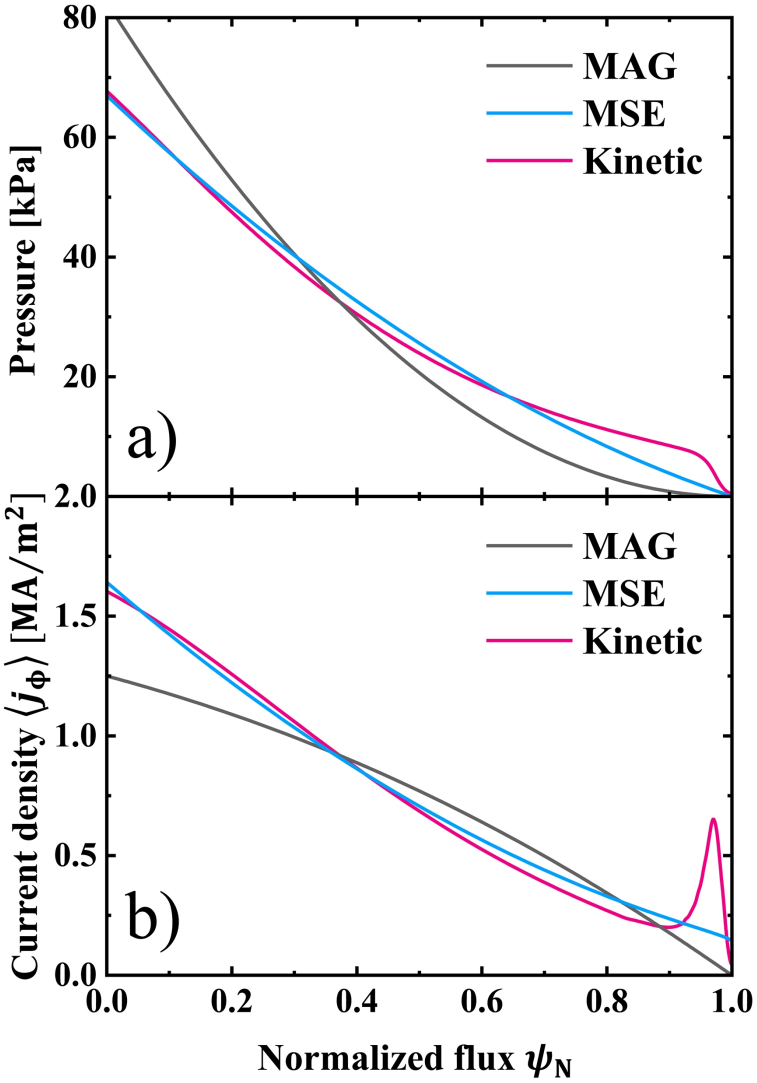

Figure 2.1: Comparison of a) the pressure and b) the current density profile of #18594, 6.45 s discharge in KSTAR. The black, blue, and red lines correspond to MAG, MSE and kinetic EFIT cases, respectively.

respectively. As more plasma diagnostics are included, the calculation result becomes more relevant to the experiment. Therefore, kinetic-EFIT is considered to be the equilibrium with the most detailed plasma information among them. For example, the comparisons between EFITs are shown in Fig.2.1. It can be found that the calculated pressure and current profiles become more accurate as more plasma measurements are included.

When evaluating the quality of plasma equilibrium, not only the number of diagnostics used in the calculation but also the numerical convergence (ϵ) and error (χ_{EFIT}) should be considered. The former means the stability of the numerical solution, while the latter corresponds to the difference between the plasma measurement and the EFIT calculation. Here, χ_{EFIT} is the sum of squared residuals. ϵ and χ_{EFIT} are enhanced with the quality of plasma diagnostics and EFIT numerical constraints. In general, $\epsilon < 10^{-9}$ and $\chi_{\mathrm{EFIT}} < 20$ have to be satisfied for advanced simulations. Therefore, it is important to obtain a high-quality equilibrium that satisfies all of the above conditions.

2.1 Obstacles in KSTAR EFIT reconstruction

Robust kinetic profiles and MSE measurements are essential components in reconstructing accurate plasma equilibria with EFIT. However, due to the limitations of the accuracy and resolution of the diagnostic system, it is challenging to obtain profiles suitable for the EFIT calculation on various devices, including KSTAR. In particular, it is hard to obtain an accurate pedestal structure near the plasma edge because of its narrow profile and technical difficulties such as low density and large-signal noise. Furthermore, MSE measurement also has considerable error-bars and bad channels that significantly increase the error in the EFIT result. Lastly, the numerical constraints in EFIT calculation are

also important. In order to obtain delicate equilibrium, it is necessary to get these parameters optimized for the target device. KSTAR needs to establish a strategy to determine them.

These obstacles in KSTAR EFIT calculation are listed in Table 2.1, which must be overcome.

Table 2.1: Summary of obstacles in KSTAR EFIT calculation

EFIT Constraints	Obstacles	Solutions
Kinetic profile	- Large error-bars - Bad Channels - Low spatial resolution at edge	- Numerical - Theoretical
MSE	- Bad Channels - Error-bars - Unavailability in some discharges	- Theoretical
Numerical Params.	- Lack of optimized parameters	- Numerical

2.2 Improvement of EFIT constraints

2.2.1 Numerical compensation

Numerical correction or compensation can be applied to improve the EFIT constraints. In KSTAR, ion temperature (T_i) and toroidal rotation (V_ϕ) are measured by charge exchange spectroscopy (CES) [28]. For electron temperature (T_e) and density (n_e), Thomson spectroscopy (TS) [7] is used. In addition, interferometry [29] and reflectometry [30] can be used to measure n_e. Because these measurements have error-bars and bad channels, it is difficult to get a smooth profile from a direct interpolation. For these reasons, a function-based

profile fitting is employed. This method fits the measured data by adjusting the coefficient of the given function. It can obtain a 1D differential profile but has the disadvantage of little freedom in the fitting. In general, as the number of coefficients increases, the degree of freedom increases.

For T_e and n_e profiles, simple profile function is used because the TS measurement has large uncertainty and low spatial resolution. This function can be written as Eq.2.1,

$$\begin{aligned} F(\psi_\mathrm{N}, \vec{a}) =& a_1 + \frac{a_2}{2\tanh 1}\left(\tanh 1 + \tanh\left[\frac{2(\psi_\mathrm{N}-1)}{a_3}+1\right]\right) \\ &+ a_4\left(1-\left(\frac{\psi_\mathrm{N}}{a_5}\right)^{a_6}\right)^{a_7} H(a_5-\psi_\mathrm{N}), \end{aligned} \tag{2.1}$$

where ψ_N is normalized poloidal flux, $\vec{a}$ are the profile coefficients, and H is the unit step function. Here, a_2 and a_3 correspond to pedestal height and width, respectively. This equation is suitable for H-mode profile data with large signal noises as it can describe the pedestal and core region at the same time and minimize numerical oscillation, although the fitting freedom is small. Because CES has relatively good quality and high spatial resolution, a profile function with more freedom, Eq.2.2, is used for T_i and V_ϕ. Here, Eq.2.2 can also describe the pedestal and core area simultaneously.

$$\begin{aligned} F(\psi_\mathrm{N}, \vec{a}) =& \frac{(a_1-a_2)}{2}\left(1+a_3\psi_\mathrm{N}+a_4\psi_\mathrm{N}^2+a_5\psi_\mathrm{N}^3\right) \\ &\times\left[1-\tanh\frac{\psi_\mathrm{N}-a_6}{a_5}\right]+a_2. \end{aligned} \tag{2.2}$$

To calculate the fitted coefficients of target function, nonlinear least square optimization scheme (LMFIT) [31] is used. By defining the least square (χ_f) as

$$\chi_{\mathrm{f}}(\vec{a}) = \sum_{\mathrm{i}}^{\mathrm{Ch.}} \frac{(F(x_{\mathrm{i}}, \vec{a}) - y_{\mathrm{i}})^2}{\sigma_{\mathrm{i}}^2}, \tag{2.3}$$

smooth profile can be obtained from measured data points $(x_{\mathrm{i}}, y_{\mathrm{i}})$. In the case of n_{e}, interferometry and reflectometry can improve the profile reconstruction. Therefore, (χ_{f}) of n_{e} profile is set to include measured 0D and 1D data from interferometry and reflectometry, respectively. It is possible to get a more experimentally relevant plasma profile with multiple diagnostics. Bad channels in measured data are excluded using an "outlier" scheme. This scheme removes any measure data point that is more than 3-sigma (standard deviation) from the initial fitting result. By repeating this scheme, the bad points can be removed, and the fitted profile improves.

The same least square method is applied to determine the numerical parameters of EFIT. They are optimized by using the LMFIT scheme to minimize the EFIT error (χ_{EFIT}), and a numerically stable equilibrium can be reconstructed. The obstacles to delicate EFIT calculation could be overcome in this way.

2.2.2 Theoretical compensation

Numerical correction can improve the problems in kinetic profiles. However, due to the low resolution of the diagnostics, it is still difficult to obtain a pedestal structure. The linear properties of PBM are used to resolve this problem. In Type I ELMy plasmas, the pedestal is known to locate near the marginal PBM stability limit [4]. 2D electron cyclotron emission imaging (ECEI) spectroscopy [32,33] captures the toroidal mode number of most unstable PBM (n_{ECEI}) in its linear phase. Based on the information of PBM, the pedestal can be adjusted from the initial profile to make it satisfy all three conditions.

Because CES has enough spatial resolution to determine the T_{i} pedestal,

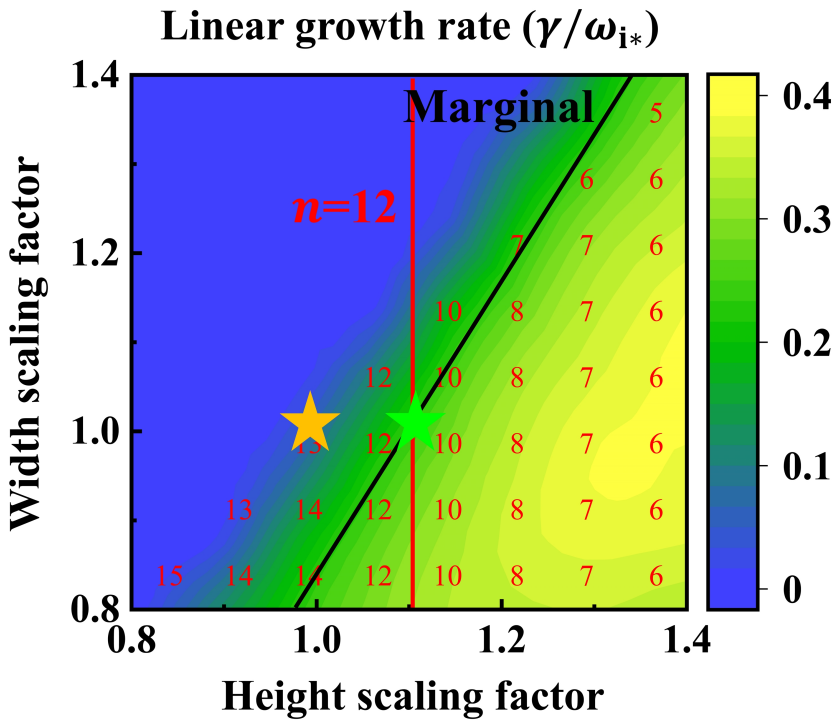

Figure 2.2: The linear growth rate of PBM of the most unstable mode in pedestal height and width space is presented. The mode number of most unstable mode is also shown. The black line is the marginal PBM stability limit, and the red line corresponds to the pedestal whose dominant PBM mode has $n = 12$. Yellow star and green star represent the reference point, the newly fitted pedestal, respectively.

only T_e and n_e need to be considered. Therefore, their pedestal width and height are scaled to see how PBM properties change. Here, the same scaling factor is applied on T_e and n_e pedestals. In this scan, the neoclassical bootstrap current is re-computed to be self-consistent with the adjusted profile. Here, the modified Sauter model [34] is used. The linear growth rate (γ) of the most unstable toroidal mode number n is checked by the ideal MHD code, MISHKA1 [35], with a simplified ion diamagnetic effect [36]. The result is shown in Fig.2.2, where #18594 (t=6450ms) KSTAR discharge is used as a reference. The orange star represents the initial pedestal, the black line is the marginal PBM stability limit ($\gamma = \omega_{i*}/4$), and the red line corresponds to the pedestal whose dominant PBM is $n = n_{\mathrm{ECEI}} = 11$. Here, ω_{i*} is the ion-diamagnetic frequency at the center of the pedestal. With this exercise, the linear instability and the most dominant n constraints are satisfied by changing the pedestal from the orange star to green star. In this way, the pedestal profile can be obtained, which is consistent with experimental and theoretical findings. We note that this approach is valid with type I ELMs.

For correction of the MSE measurement, the plasma current models are employed. When the last closed flux surface (LCFS) of MAG-EFIT is given, a model-based plasma equilibrium can be generated using a fixed boundary equilibrium solver (FBE) with kinetic profiles and plasma current models. With the magnetic field information ($\vec{B}$) of this equilibrium, the synthetic MSE data, γ_{MSE}, can be numerically reconstructed, which can correct the measured data. The CHEASE code [37] is used as FBE. The plasma current profile ($j_{\parallel}$) and γ_{MSE} are calculated from Eq.2.4 and Eq.2.5, respectively.

$$\langle j_{\parallel} B \rangle = \alpha_{\mathrm{OH}} \left\langle \frac{\sigma_c}{R^2} \right\rangle + \langle j_{\mathrm{BS}} B \rangle + \langle j_{\mathrm{EXT}} B \rangle \tag{2.4}$$

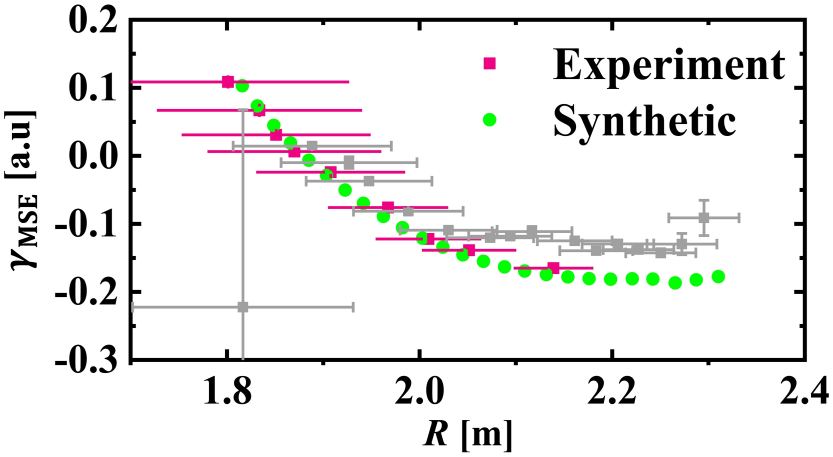

Figure 2.3: Comparison between experimental and synthetic MSE data. The red points are selected MSE channels, while the gray points are determined as bad channels by comparison.

$$\gamma_{\mathrm{MSE}} = \frac{A_1 B_{\mathrm{Z}}}{A_2 B_\phi + A_3 B_{\mathrm{R}} + A_4 B_{\mathrm{Z}}} \tag{2.5}$$

Here, $\langle .. \rangle$ refers to flux surface average, σ_c is the plasma conductivity, R is the major radius, α_{OH} is the ohmic current coefficient, j_{BS} is the bootstrap current, and j_{EXT} is the external driven plasma current. σ_c and j_{BS} are derived from Refs. [12, 34], while j_{EXT} is calculated by using the NUBEAM [38] and TORAY [39] codes. α_{OH} is determined to satisfy the measured total plasma current. In Eq.2.5, $\vec{B}$ is expressed in cylindrical coordinate (R, Z, ϕ), and A_{i} are the geometrical coefficients, which depends on the device configuration. Their expressions can be found in Ref. [40]

An example of synthetic MSE is shown in Fig.2.3. The KSTAR plasma discharge of #21072 (t=4950 ms) is used as a reference. In the core region, the synthetic and measured values show good agreement, whereas, in the edge re-

gion, a considerable difference occurs. Because the MSE diagnostic tends to be less accurate in the outer region, the synthetic MSE can be neglected in this region. Here, the measured points showing a large difference from the synthetic data are judged as bad channels and excluded. By selecting and removing the bad channels, the χ_{EFIT} is significantly reduced from 33 to 16.4. This outcome supports the validity and effectiveness of the above strategy. Furthermore, synthetic MSE can replace measurement values in cases where the MSE diagnostic is missing. It dramatically expands the possibility of plasma analyses. We note that this approach is valid in stationary conditions, where the ohmic current profile is fully developed.

2.3 Kinetic EFIT reconstruction in KSTAR

Delicate numerical equilibrium is essential for a physics study of KSTAR plasmas. Because of obstacles in KSTAR EFIT reconstruction, many corrections and schemes are needed. Therefore, it is worthwhile to make an integrated toolkit for EFIT calculations in KSTAR. The GEFIT toolkit was developed for high-quality kinetic EFIT reconstructions, and it is used to generate the reference plasma equilibrium for nonlinear MHD analysis of the RMP effect.

2.3.1 GEFIT toolkit

Numerical and theoretical compensation schemes in the above section take a lot of numerical calculations and post-processings. A GUI-based kinetic-EFIT toolkit, GEFIT, supports a user-friendly environment to generate EFIT effectively. This toolkit contains profile fitting, equilibrium, and linear PBM stability analysis tools. The structure and interface of GEFIT are shown in Fig.2.4. The Python framework connects CHEASE, MISHKA, NUBEAM, TORAY, and

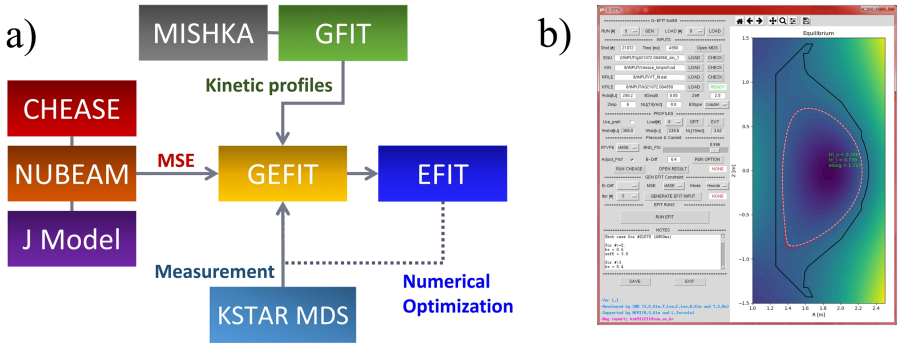

Figure 2.4: a) Code structure and b) graphical user interface of GEFIT toolkit

EFIT codes. For user convenience, the KSTAR data server is connected to the code so that the experiment data can be quickly loaded. Plasma current models and numerical schemes are also implemented in GEFIT. By using this tool, the kinetic-EFIT can be obtained.

2.3.2 Reference equilibrium

This study uses the data from KSTAR #18594 discharge [25] of $n = 2$ RMP-driven ELM suppression. The overview of this discharge is shown in Fig.2.5; plasma current ($I_{\mathrm{p}} = 0.66$ MA), stored energy ($W_{\mathrm{MHD}} = 0.43$ MJ), and line average density ($\bar{n}_{\mathrm{e}} \sim 3.3 \times 10^{19}\mathrm{m}^{-3}$). In addition, its main parameters are; major radius ($R_0 = 1.8$ m), toroidal field ($B_{\phi 0} = 1.8$ T), q profile with central $q_0(\sim 1)$, $q_{95}(\sim 4.0)$, and global poloidal beta ($\beta_{\mathrm{p}} \sim 1$). In this discharge, the currents in the three rows of versatile in-vessel control coils (IVCC) with two turns in the low field side [5] were set such that the magnetic perturbation of $n = 2$ was applied. The phase difference between the rows was $\Delta\phi = 90°$, and it is the standard $n = 2$ field coil configuration for suppressing ELMs in KSTAR. When the stationary state was reached (~ 4.9 s), RMP with the coil current $I_{\mathrm{RMP}} = 2$ kA was applied from 5.0 s to 5.5 s and then gradually increased

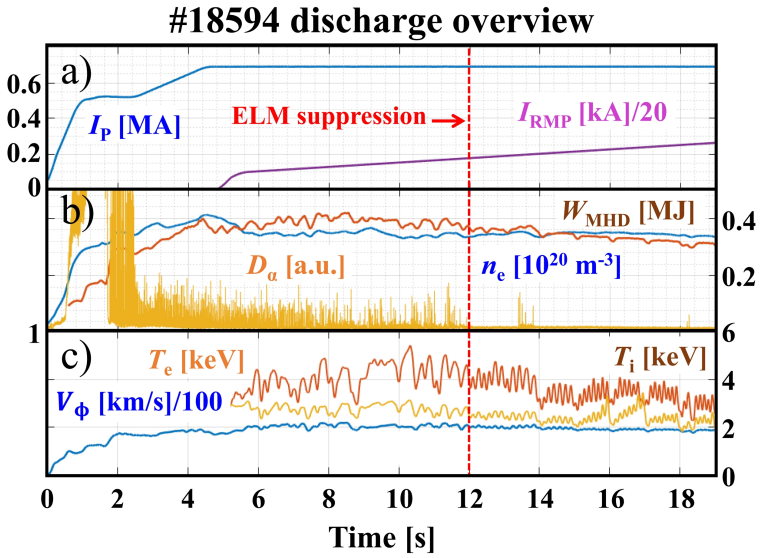

Figure 2.5: Time evolution of (a) plasma current, I_{p}, RMP coil current, I_{RMP}, (b) D_α signal, line average density, $\bar{n}_{\mathrm{e}}$, (c) ion temperature, T_{i}, electron temperature, T_{e}, and toroidal plasma rotation, V_ϕ in core of the KSTAR discharge #18594.

with the rate of ∼0.2 kA/s. ELM suppression was achieved at 13.0 s with $I_{\mathrm{RMP}} \sim 3.7$ kA. This full suppression lasted until the end of the discharge. We note that I_{RMP} is defined as twice the current applied in the actual experiment because the coil is wound in two turns. In this study, $t = 6.45$ s, the earliest time slice when ECEI measurement becomes available, is selected as a reference time. At this point, the profile variation and ELM mitigation by RMP have not yet appeared. For this time-slice, the plasma equilibrium is reproduced, and simulation results are compared with the ECEI measurement.

The axisymmetric equilibrium is reconstructed with GEFIT. Its q, kinetic, and current profiles are presented in Fig.2.6. Because $\epsilon = 10^{-12}$ and $\chi_{\mathrm{EFIT}} = 16.3$, it is confirmed that the reconstructed EFIT equilibrium is enough for nonlinear MHD simulations. It is noteworthy that the tokamak system becomes no longer axisymmetric when 3D fields are applied. So 3D equilibrium reconstruction of the tokamak is also valuable for the study on the effect of RMP [41–43], which could be included in future work.

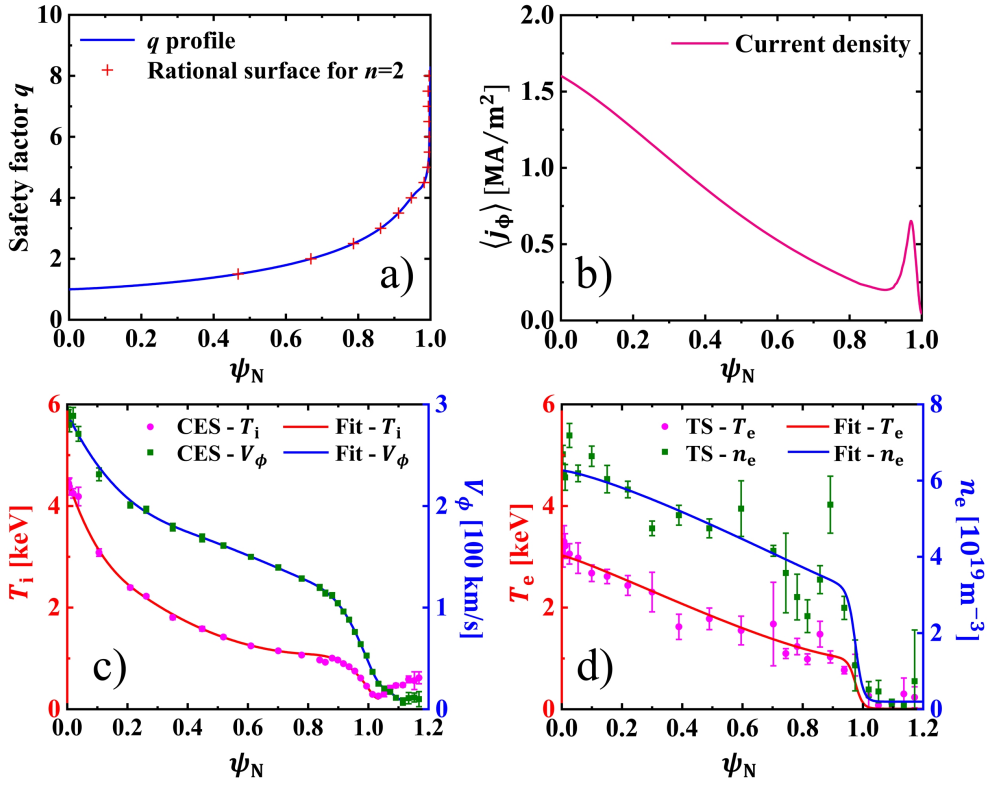

Figure 2.6: (a) Radial profile of safety factor q (blue line) and position of rational surface (red dot) with $n = 2$. (b) Radial profile of flux averaged current density $\langle j_\phi \rangle$ (red line). (c) Radial profiles of electron temperature, T_e (red line), and electron density, n_e, (blue line) taken in modeling, with the experimental measurements of T_e (red dot) and n_e (green dot). (d) Radial profiles of ion temperature, T_i (red line), and toroidal rotation velocity, V_ϕ (blue line), taken in modeling, with the experimental measurements of T_i (red dot) and V_ϕ (green dot).

Chapter 3

RMP-driven Plasma response

The RMP-driven equilibrium responses are highly responsible for ELM suppression. In particular, they affect pedestal transport. For example, the pedestal degradation is commonly observed as a consequence of RMP application. Because an initial understanding of the ELM suppression is based on the pedestal degradation due to the formation of the stochastic layer, extensive research on field penetration and radial transport by RMPs have been carried out. They have revealed that perpendicular electron flow shields RMPs and a zero electron flow layer ($\omega_{\perp,\mathrm{e}} \approx 0$) [44–46] is important for full field penetration in the pedestal. Numerical studies have shown that RMPs can drive a kink-peeling response [47,48] in the plasma and amplify field penetration [49]. We note that the collisional thermal transport in the stochastic layer is larger than that of particle. However these approach have limitations in explaining the experimental observation where the degradation in the density pedestal is much larger than temperature pedestal. In addition, most previous studies are limited to

the linear analysis. The equilibrium responses including field re-connection are no longer a linear phenomena, so nonlinear studies are needed.

3.1 Numerical analysis tools

For the numerical analysis on the plasma response, the nonlinear MHD code, JOREK [50], and the 3D vacuum field code, ERGOS [51], are employed.

3.1.1 JOREK

JOREK is a 3D nonlinear MHD code with X-points and scrape-off-layer (SOL). The reduced MHD model based on five field equations is used, including Ohm's law, the continuity equation, the momentum equation, and the energy equation. Momentum equations are divided into parallel and perpendicular components. The realistic toroidal flow, two-fluid diamagnetic effect, and the neoclassical viscosity are included to describe the effect of plasma flow on the ballooning modes [45, 52].

In the JOREK code, the magnetic field is expressed as $\vec{B} = F_0 \nabla\phi + \nabla\psi \times \nabla\phi$, where ϕ is the toroidal angle, ψ is the poloidal magnetic flux, and $F_0 = R_0 B_{\phi 0}$. R_0 is the magnetic axis, and $B_{\phi 0}$ is the amplitude of the toroidal field at $R = R_0$. F_0 is constant in time, and ϕ increases clockwise in the simulation.

The plasma fluid velocity $\vec{V}$ is expressed as Eq.3.1

$$\vec{V} = \vec{V}_{\parallel} + \vec{V}_{\mathrm{E}} + \vec{V}_{\mathrm{i}*} \tag{3.1}$$

where $\vec{V}_{\parallel}$ is the velocity parallel to the magnetic field, and $\vec{V}_{\mathrm{E}} = \vec{E} \times \vec{B}/B^2$ is the $\vec{E} \times \vec{B}$ drift velocity. The electric field is expressed as $\vec{E} = -\nabla u$ where u is the electrostatic potential. $\vec{V}_{\mathrm{i}*} = -\nabla P_{\mathrm{i}} \times \vec{B}/(\rho e B^2/m_{\mathrm{i}})$ is the ion diamagnetic velocity that reflects the two-fluid diamagnetic effect. Here, P_{i}, e, m_{i}, and

$\rho(= m_{\rm i} \times n_{\rm i})$ are the scalar pressure, charge, mass, and mass density of ion, respectively. The density of ion and electron is assumed to be $n_{\rm i} = n_{\rm e}$. We also set $T_{\rm i} = T_{\rm e} = T/2$ and $P_{\rm i} = P_{\rm e} = P/2$ for simplicity, where T and P are the sum of ion and the electron temperatures and scalar pressures, respectively. The normalized set of five field equations [52] is:

$$\frac{1}{R^2}\frac{\partial \psi}{\partial t} = -\vec{B}\cdot\left(\nabla u - \frac{\tau_{\rm IC}}{\rho}P\right) + \eta\nabla\cdot\left(\frac{1}{R^2}\nabla_\perp\psi - j_{\rm s}\right), \tag{3.2}$$

$$\frac{\partial \rho}{\partial t} = -\nabla\cdot\left(\rho\vec{V}\right) + \nabla\cdot\left(D_\perp\nabla_\perp\rho\right) + S_\rho, \tag{3.3}$$

$$\nabla\phi\cdot\nabla\times R^2\begin{bmatrix}\rho\left(\partial_{\rm t} + \vec{V}\cdot\nabla\right)\vec{V}_{\rm E} + \nabla\left(\rho T\right) - \vec{j}\times\vec{B}\\ +\nabla\cdot\bar{\Pi}_{\rm i,neo} - \vec{S}_{\rm V} + \vec{V}S_\rho - \nu_\perp\nabla^2\vec{V}\end{bmatrix} = 0, \tag{3.4}$$

$$\vec{B}\cdot\begin{bmatrix}\rho\left(\partial_{\rm t} + \vec{V}\cdot\nabla\right)\vec{V}_{\parallel} + \nabla\left(\rho T\right) - \vec{j}\times\vec{B}\\ +\nabla\cdot\bar{\Pi}_{\rm i,neo} - \vec{S}_{\rm V} + \vec{V}S_\rho - \nu_\perp\nabla^2\vec{V}\end{bmatrix} = 0, \tag{3.5}$$

$$\begin{aligned}\frac{\partial\left(\rho T\right)}{\partial t} =& -\left(\vec{V}_{\rm E} + \vec{V}_{\parallel}\right)\cdot\left(\rho T\right) - \gamma\rho T\nabla\cdot\left(\vec{V}_{\rm E} + \vec{V}_{\parallel}\right)\\ &+ \nabla\cdot\left(\rho\kappa_\perp\nabla_\perp T + \rho\kappa_\parallel\nabla_\parallel T\right) + \left(1-\gamma\right)S_{\rm T} + V^2 S_\rho/2.\end{aligned} \tag{3.6}$$

The variables are normalized as follows: $\rho = \rho_{\rm SI}/\rho_{0,\rm SI}$ and $t = t_{\rm SI}/\sqrt{\mu_0\rho_{0,\rm SI}}$, where SI represents the SI unit value, $\mu_0 = 4\times10^{-7}$, and $\rho_{0,\rm SI}$ is mass density on the magnetic axis. The normalization of the other variables is $P = \mu_0 P_{\rm SI}$, $T = \mu_0\rho_{0,\rm SI}(e/m_{\rm i})T_{\rm SI}$, $j = \mu_0 j_{\rm SI}$, and $u = u_{\rm SI}\sqrt{\mu_0\rho_0}/F_{0,\rm SI}$. j is the plasma current density. The flow is normalized to $V_\parallel = V_{\parallel,\rm SI}\sqrt{\mu_0\rho_0}/B_{\rm SI}$ and $V_\theta = \vec{V}\cdot\hat{e}_\theta = V_{\theta,\rm SI}/\sqrt{\mu_0\rho_0}$, depending on the direction. Here, the poloidal unit vector $\hat{e}_\theta$ is defined as

$$\hat{e}_\theta = \frac{R}{\nabla\psi}\left(\nabla\psi \times \nabla\phi\right). \tag{3.7}$$

A Spitzer-like resistivity $\eta = \eta_{0,\mathrm{SI}}\sqrt{\rho_{0,\mathrm{SI}}/\mu_0}\left(T_\mathrm{e}/T_{\mathrm{e},0}\right)^{-3/2}$, temperature-dependent perpendicular viscosity $\nu_\perp = \nu_{\perp 0,\mathrm{SI}}\sqrt{\mu_0/\rho_{0,\mathrm{SI}}}\left(T_\mathrm{e}/T_{\mathrm{e},0}\right)^{-3/2}$, and constant parallel viscosity $\nu_\parallel = \nu_{\parallel,\mathrm{SI}}\sqrt{\mu_0/\rho_{0,\mathrm{SI}}}$ are used in the modeling. Here, $\eta_{0,\mathrm{SI}}, \nu_{\perp 0,\mathrm{SI}}$, and $T_{\mathrm{e},0}$ are the resistivity, perpendicular viscosity, and electron temperature on the magnetic axis, respectively. Braginskii parallel conductivity $\kappa_\parallel$=$\kappa_{\parallel 0,\mathrm{SI}}\sqrt{\mu_0/\rho_{0,\mathrm{SI}}}$ $\left(T_\mathrm{e}/T_{\mathrm{e},0}\right)^{5/2}$ and adiabatic index $\gamma = 5/3$ are also applied. Particle source S_ρ and the heat source S_T, as well as the perpendicular particle diffusion coefficient $D_\perp = D_{\perp\mathrm{SI}}\sqrt{\rho_{0,\mathrm{SI}}\mu_0}$ and thermal diffusion coefficient $\kappa_\perp = \kappa_{\perp\mathrm{SI}}\sqrt{\mu_0/\rho_{0,\mathrm{SI}}}$ are set to maintain the initial density and temperature profiles. Their typical values on the magnetic axis are $D_{\perp 0,\mathrm{SI}} \approx 1\mathrm{m}^2\mathrm{s}^{-1}$ and $\kappa_{\perp 0,\mathrm{SI}}/\rho_{\perp 0,\mathrm{SI}} \approx 1\mathrm{m}^2\mathrm{s}^{-1}$. $D_\perp$ and $\kappa_\perp$ vary radially. Their radial profiles are proportional to $D_\perp \propto |\nabla\rho|^{-1}$ and $\kappa_\perp \propto |\nabla T|^{-1}$ of initial ρ and T profiles. In addition, the current source j_s and the toroidal momentum source $\vec{S}_\mathrm{V}$ are applied to reproduce the realistic equilibrium profile. All source profiles remain the same over time.

The neoclassical poloidal friction has the heuristic form [53] as

$$\nabla\cdot\bar{\Pi}_{\mathrm{i,neo}} = \rho\mu_{\mathrm{i,neo}}\frac{B^2}{B_\theta^2}\left(V_\theta - V_{\theta,\mathrm{neo}}\right)\hat{e}_\theta, \tag{3.8}$$

where $B_\theta = \vec{B}\cdot\hat{e}_\theta$, $V_{\theta,\mathrm{neo}} = k_\mathrm{i}\tau_\mathrm{IC}\left(\nabla_\perp\psi\cdot\nabla_\perp T\right)/B_\theta$, $\mu_{\mathrm{i,neo}} = \mu_{\mathrm{i,neo,SI}}\sqrt{\mu_0\rho_0}$, and $\tau_\mathrm{IC} = m_\mathrm{i}/\left(2eF_0\sqrt{\mu_0\rho_0}\right)$. The neoclassical coefficients $\mu_{\mathrm{i,neo}}$ and k_i are calculated from Ref [54]. Using these models, the plasma flows develop toward equilibrium, and plasma is finally obtained in which the flows and electric field satisfy the radial force balance. The radial electric field can be written as Eq.3.9 [55], where ∂_r is the radial gradient and V_ϕ is the toroidal plasma flow.

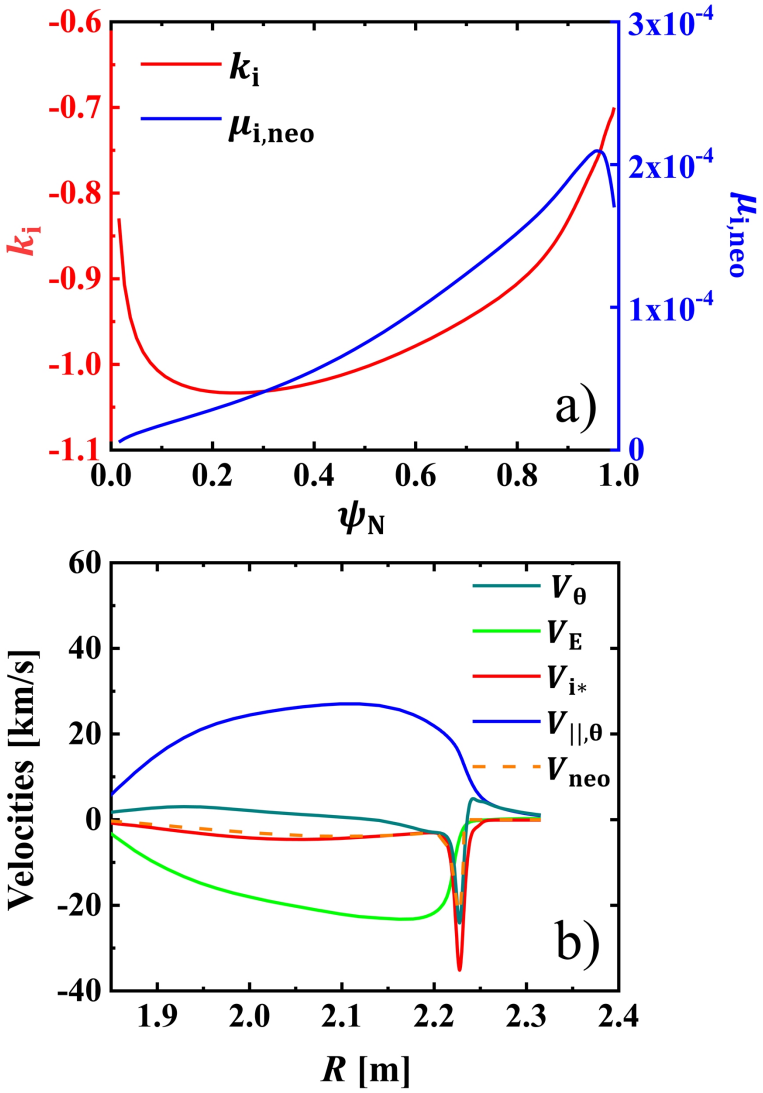

Figure 3.1: Comparison of (a) Radial profiles of neoclassical coefficients, k_i (red line) and $\mu_\mathrm{i,neo}$ (blue line). (b) Radial profiles of poloidal velocity V_θ at the midplane of LFS with $E \times B$ (V_E, green line), ion diamagnetic ($V_{\mathrm{i}*}$, red line), parallel ($V_{\|,\theta}$, blue line), and neoclassical (V_neo, orange line) components.

$$E_{\mathrm{r}} = \frac{1}{en}\frac{\partial P_{\mathrm{i}}}{\partial r} + B_\phi V_\theta - B_\theta V_\phi \tag{3.9}$$

Based on Eqns.3.8 and 3.9, the neoclassical flow and E_{r} of reference equilibrium are calculated. The neoclassical coefficients and the poloidal flow profiles from the resulting E_{r} are shown in Fig.3.1. The self-consistent kinetic equilibrium with plasma flow based on experimental data can be reproduced in this way.

In JOREK, 2D cubic Bezier finite elements are used to reconstruct a 2D grid in a poloidal cross-section [56], and the toroidal direction is decomposed into the Fourier series. Finite element grids align to equilibrium flux surfaces that include core, SOL, and the private region. The boundary of the computational domain is limited by the flux surfaces and divertor target plates. For the boundary condition of the computational domain, the Dirichlet condition is used for all variables except the divertor targets. On the divertor targets, the temperature and the density have free outflow, and Bohm sheath boundary conditions are applied [55]. The implicit Crank–Nicolson scheme is used for time stepping. The sparse system of equations is solved using Generalized Minimal REsidual Solver (GMRES) with a preconditioner obtained by solving each submatrix independently corresponding to non-coupled Fourier harmonics. These sub-matrices are solved using PaStiX [57], the direct parallel sparse matrix solver.

3.1.2 ERGOS

ERGOS is a numerical code for 3D vacuum field calculation. It derives the magnetic vector potential, $\vec{A}_{\mathrm{RMP}}$, for the given coil current configuration with Biot-Savart law, Eq.3.10.

$$\vec{A}_{\mathrm{RMP}} = \frac{\mu_0}{4\pi} \sum_{\mathrm{c}} \int \frac{I_{\mathrm{c}}}{r_{\mathrm{c}}} d\vec{l_{\mathrm{c}}} \tag{3.10}$$

Here,"c" denotes the coils, I_{c} is the coil current, dl_{c} is the length, and r_{c} is the distance to its location. Then, the perturbation of poloidal flux due to vacuum RMP field, $\delta\psi_{\mathrm{RMP}}$, can be expressed as Eq.3.11.

$$R^2 \nabla\phi \times \left(\nabla \times \vec{A}_{\mathrm{RMP}} \right) \cong \nabla \left(R A_{\mathrm{RMP},\phi} \right) = \nabla \left(\delta\psi_{\mathrm{RMP}} \right) \tag{3.11}$$

In this study, $\delta\psi_{\mathrm{RMP}}$ is toroidally decomposed into the Fourier series and numerically included in JOREK for the RMP simulation. Due to the geometry of IVCC, small sideband modes such as $n = 4, 6, 8$, etc., also exist in experiments, but they are ignored in simulations because they are much smaller than the amplitude of the $n = 2$ component.

3.1.3 Numerical modeling of RMP

RMP in JOREK simulations is treated with a similar approach as in [52]. ERGOS calculates $\delta\psi_{\mathrm{RMP}}$ for a given configuration. The calculation result for $\delta\psi_{\mathrm{RMP}}$ is presented in Fig.3.2. $\delta\psi_{\mathrm{RMP}}$ is applied as a modified boundary condition in the JOREK computational domain. It is based on the vacuum approximation as the boundary of the computational domain is far from the main plasma. The perturbed boundary condition is gradually established during $300\tau_{\mathrm{A}}$. Then, the plasma response after $\sim 1000\tau_{\mathrm{A}}$ is considered as the RMP-driven equilibrium response, where the numerical convergence is achieved. The schematic diagram of the RMP modeling process is presented in Fig.3.3. In this way, the penetration of RMP into the plasma is evaluated self-consistently.

As the plasma equilibrium response by RMP is investigated in this section, only $n = 0$ (equilibrium) and $n = 2$ (RMP) harmonics are included in the

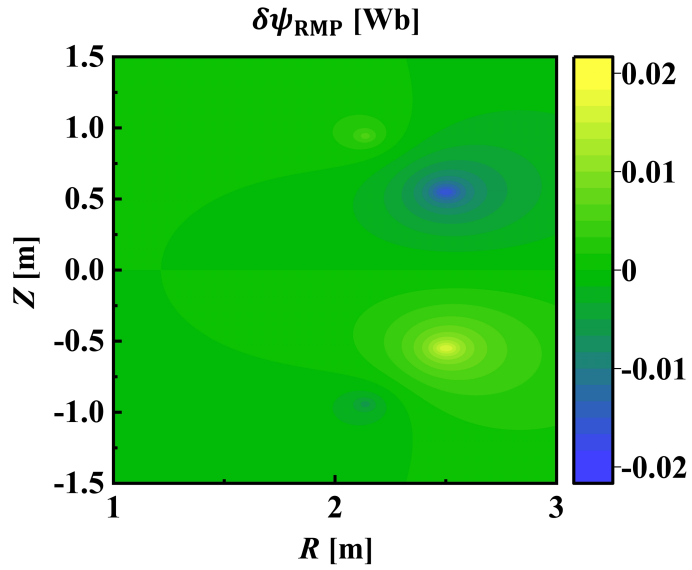

Figure 3.2: 2D distribution of perturbed poloidal flux, $\delta\psi_{\mathrm{RMP}}$, on $R-Z$ space. $n=2$ component of ψ_{RMP} is shown here.

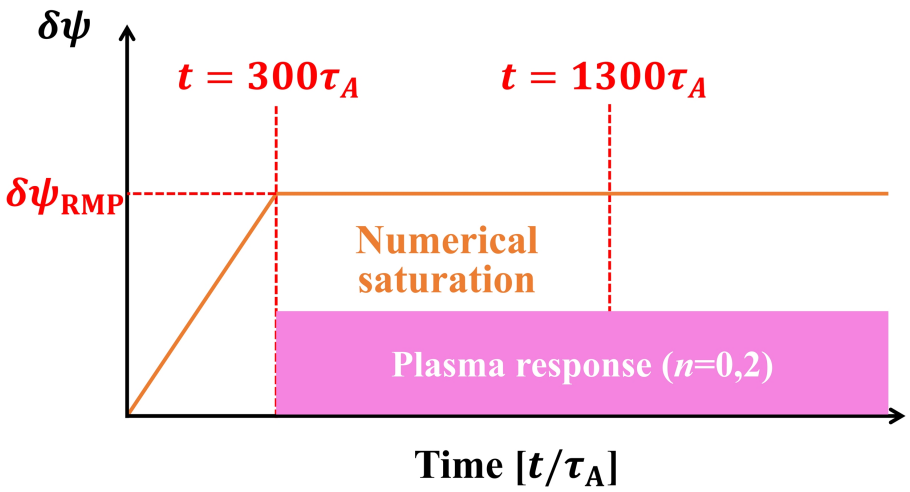

Figure 3.3: Schematic diagram for the numerical modeling of RMP application in JOREK simulation.

modeling. Here, I consider an $n = 2$ plasma response as a harmonic component that is different from the main PBM. In addition, we used normalized JOREK parameters based on the experimental data; $\kappa_{\parallel,0} = 2 \times 10^3$ ($\kappa_{\parallel 0,\mathrm{SI}} = 7.02 \times 10^2$ kg $\cdot$ m^{-1}s^{-1}), $\nu_{\perp 0} = 2 \times 10^{-7}$ ($\nu_{\perp 0,\mathrm{SI}} = 7.02 \times 10^{-8}$ kg $\cdot$ m^{-1}s^{-1}), and $\nu_{\parallel} = 2 \times 10^{-6}$ ($\nu_{\parallel,\mathrm{SI}} = 7.02 \times 10^{-7}$ kg $\cdot$ m^{-1}s^{-1}). Here, for numerical reasons, 40 times larger resistivity ($\eta_0 = 2 \times 10^{-7}$, $\eta_{0,\mathrm{SI}} = 5.7 \times 10^{-7}\Omega$m) and two times smaller τ_{IC} ($=3 \times 10^{-3}$) are used, and it is one of the important limitations of this study.

3.2 Plasma response

The simulation shows a nonlinear plasma response, including changes of both $n = 0$ and $n = 2$ components. This response can be separated into the kink and the tearing components.

3.2.1 Kink response

When RMP is established, the plasma perturbations are observed. The perturbed poloidal flux, density, and temperature are presented in Fig.3.4 (a), (b), and (c), respectively. As RMP penetrates the plasma, $n = 2$ perturbations with $m = 7 - 14$ occur in the edge region. Larger perturbations of temperature and density are observed at the X-point. In order to identify this response, the linear displacement $\xi_{\perp,\mathrm{lin}}$ is calculated from Ref [47], and this mode has an edge localized structure as shown in 3.5 with kink-peeling mode (KPM) characteristics [47, 49, 58, 59]. Note that the $n = 2$ mode is linearly stable without RMPs so it is sure that RMPs linearly drive the $n = 2$ KPM. This result is consistent with the previous studies where peeling-like modes were observed in the response under RMP [60–62].

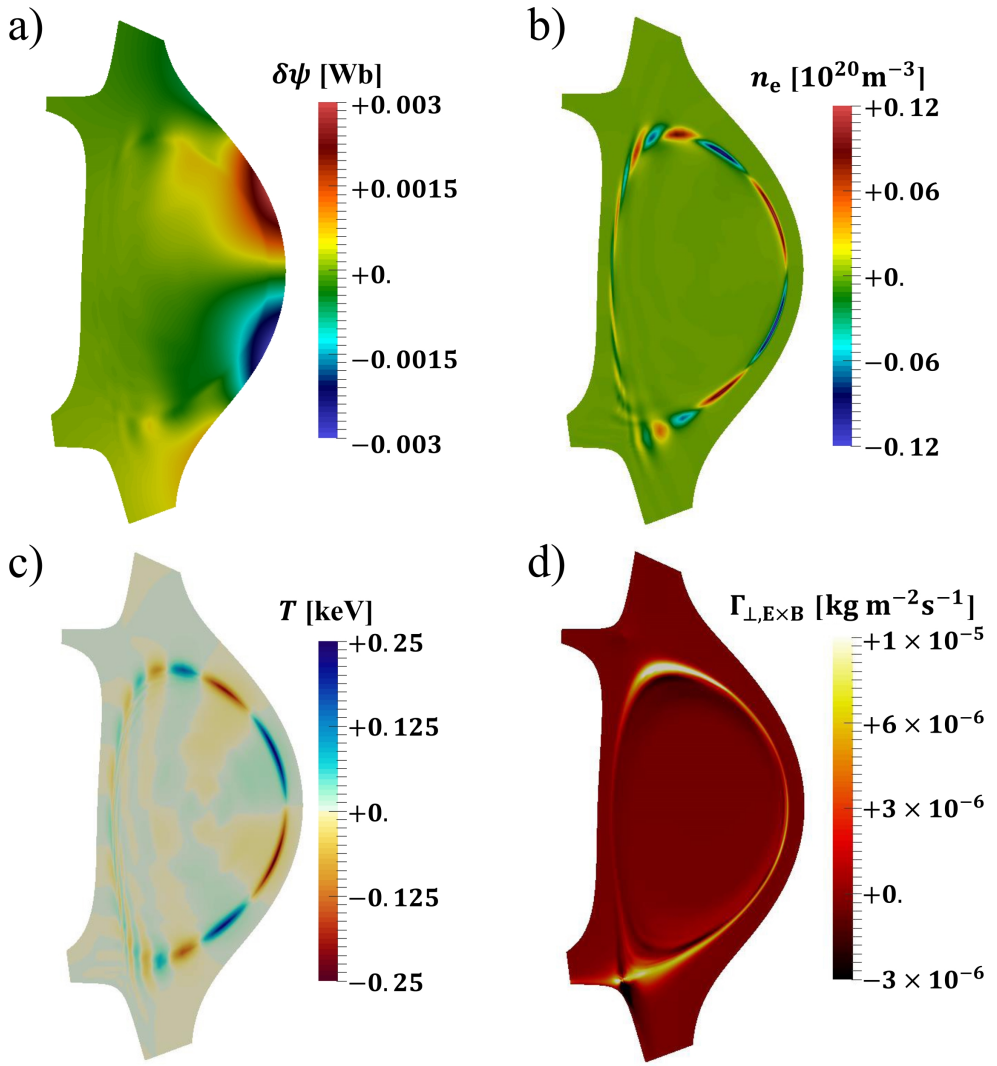

Figure 3.4: 2D poloidal distribution of (a) $n = 2$ magnetic flux $\delta\psi$, (b) n_e, and (c) T perturbation induced by RMP. (d) $n = 0$ $E \times B$ radial flux, $\Gamma_{\perp,E\times B}$, which is driven by the RMP-induced plasma response.

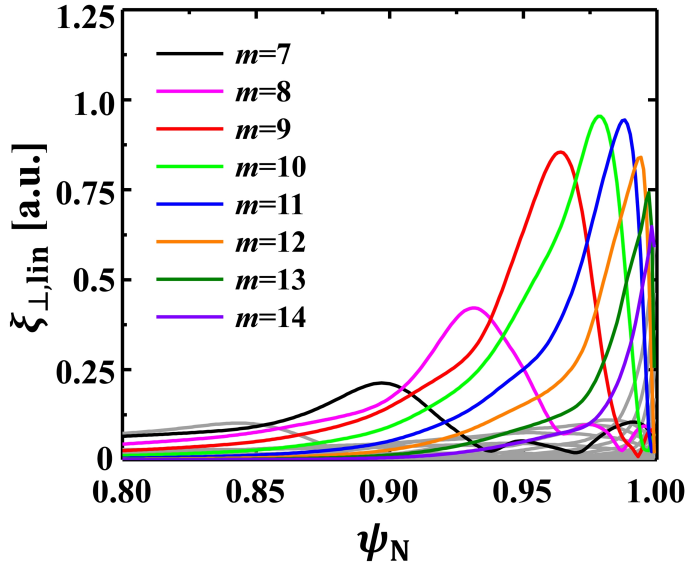

Figure 3.5: Radial mode structure of the plasma displacement $\xi_{\perp,\mathrm{lin}}$ induced as a response to RMP. The mode structure is highly localized at the plasma edge, which is the typical structure of KPM.

Interestingly, a perturbed radial E×B flow is generated at the edge region due to KPM. It results in $n = 0$ convective flux, $\Gamma_{\mathrm{E\times B}}$, in the radial direction. The distribution of $\Gamma_{\mathrm{E\times B}}$ driven by KPM can be found in Fig.3.4(d). A large $\Gamma_{\mathrm{E\times B}}$ layer exists at $\psi_{\mathrm{N}} = 0.98 - 1.0$ and is widely distributed poloidally. It has the largest value near the X-point, which agrees with the mode structure of KPM. This widely distributed $\Gamma_{\mathrm{E\times B}}$ increases radial transport in the pedestal. The formation of the particle and heat convection flux is also consistent with similar numerical studies [63, 64].

3.2.2 Tearing response

In addition to the KPM-like plasma response, magnetic islands can be formed due to RMP field penetration. However, the plasma shielding current that suppresses the field penetration can be generated, which reduces the island size. This shielding effect is the result of the plasma flow and the low resistivity of the core plasma [44–46, 65–67]. RMP cannot penetrate the plasma when plasma has zero resistivity or infinite rotation [58, 68]. The calculated field penetration is given in Fig.3.6. Fourier decomposed perturbed poloidal flux (Fig.3.6(a)) and the plasma current (Fig.3.6(b)) are plotted on the poloidal mode number versus ψ_{N} space. The field penetration is almost blocked on the rational surface (red line) due to the formation of the shielding current at each resonant surface. Therefore, only small islands remain in the core region.

On the other hand, significant field penetration is observed in the edge region. Because plasma resistivity is relatively large in this region, the perturbed current cannot entirely shield the external field [45]. We note that the field penetration may vary depending on the resistivity used in the simulation. Also, a layer with zero perpendicular flow, $V_{\perp,\mathrm{e}} \approx 0$, exists at the rational surface near

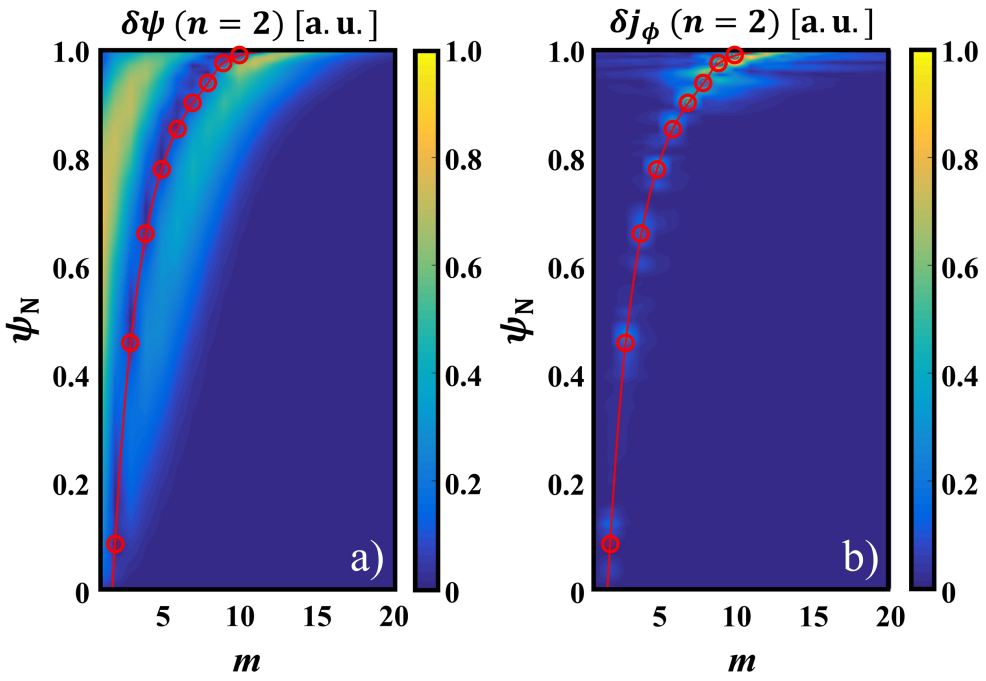

Figure 3.6: Perturbed $n = 2$ components of the (a) poloidal magnetic flux $\delta\psi$ and (b) current δj_ϕ as functions of the poloidal mode number m and the normalized flux ψ_{N} are presented. In each figure, resonant surfaces are plotted with the red line and circles.

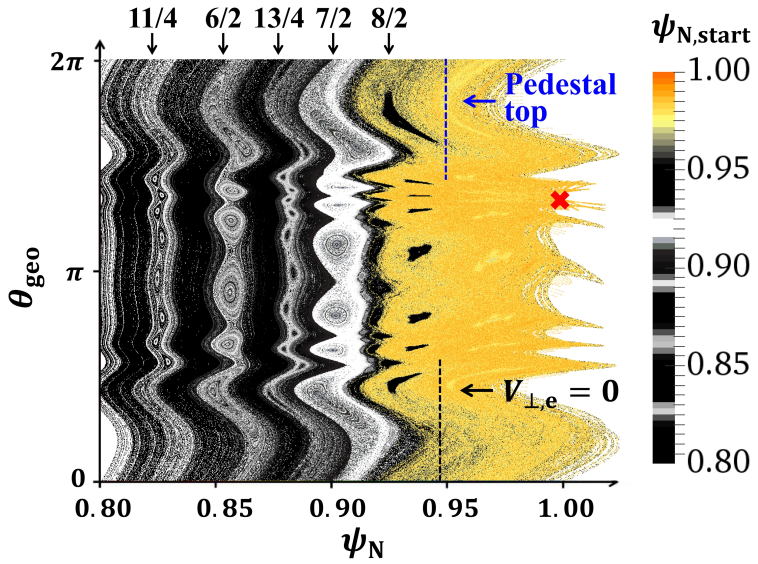

Figure 3.7: Poincare plot of the perturbed magnetic structure in ψ_{N} and poloidal θ_{geo} coordinate is presented. The stochastic layer is formed at $0.95 \leq \psi_{\mathrm{N}} \leq 1.0$. Here, the color values represent ψ_{N} of the starting point of field line tracing. The positions of pedestal top, $V_{\perp,\mathrm{e}} = 0$, and X-point are represented by the blue dotted line, black dotted line, and red cross, respectively.

$\psi_N = 0.95$ which corresponds to the pedestal top in our case. The external field can fully penetrate into this region [46, 52, 65, 67] and generate large magnetic islands. Furthermore, the magnetic perturbation is amplified by the poloidal coupling with the kink component, and KPM enhances the field reconnection at the plasma boundary [49, 69]. Therefore, the large island can remain in the pedestal region, and the stochastic layer is formed by the overlap of islands. This can be clarified in the Poincare plot in Fig.3.7. Here, θ_{geo} is defined as

$$\theta_{\mathrm{geo}} = \arctan\left[\frac{Z - Z_0}{R - R_0}\right], \tag{3.12}$$

where Z_0 is the location of the magnetic axis in the (R, Z) coordinate. In this plot, large island structures at the resonant surfaces ($q = 7/2$ and $8/2$) near the pedestal top are found while the island size at the inner region ($q = 6/2$) is much smaller. A secondary island structure is also generated at $q = 11/4$. For $0.95 \leq \psi_N \leq 1.0$, the stochastic layer exists, which can increase the radial transport. In this work, the radial transport in the stochastic layer can increase due to the parallel transport described by the Braginskii model.

3.3 Increased pedestal transport

KPM and the magnetic islands occur as a plasma response under the external field perturbation. They generate the convection cells and a stochastic layer in the pedestal region, which can lead to increased radial transport. In addition, neoclassical toroidal viscosity (NTV) can be driven due to the symmetry breaking [70, 71], which can induce further pedestal transport.

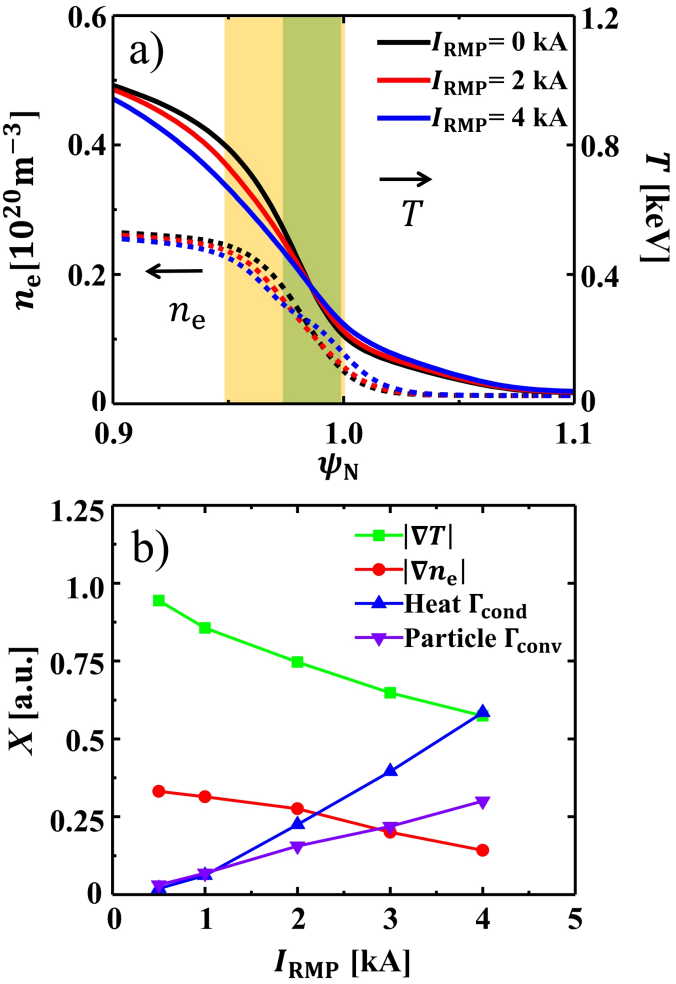

Figure 3.8: (a) $n = 0$ profile degradation of n_e and T pedestal, which is induced by RMP. The yellow and green colored regions highlight the radial width of the stochastic layer and $E \times B$ convection layer, respectively. (b) The radial gradient of n_e (red dotted line) and T (blue dotted line) at the center of the pedestal ($\psi_N = 0.98$) with varying I_{RMP}. The conductive heat flux Γ_{cond} and convective particle flux Γ_{conv} at the same location are also presented.

3.3.1 Kink-tearing response driven transport

Increased radial transport due to tearing and kink-peeling response to RMP can lead to the degradation of the mean ($n = 0$) pedestal gradient and stabilization of edge MHD modes. To investigate the variation of the mean profile under RMP, plasma responses to $0 \leq I_{\mathrm{RMP}} \leq 4$ kA are calculated. Fig.3.8(a) shows the degradation of mean pedestal profiles of the density and the temperature. As the amplitude of the RMP field increases, the gradient of both n_{e} and T pedestal decreases. For example, ∇n_{e} and ∇T at the center of the pedestal ($\psi_{\mathrm{N}} = 0.98$) decrease by 58% and 39%, respectively, as $I_{\mathrm{RMP}} = 4$ kA is applied. Here, the yellow and the green colored region correspond to the stochastic layer and the location of the convection ($\Gamma_{\mathrm{E\times B}}$) layer at the mid-plane of LFS, respectively.

The overall degradation of the n_{e} and T pedestals appears in the stochastic layer because of the increased radial transport. In the convection layer, on the other hand, the change in n_{e} pedestal is significant while that of T pedestal is small. This implies that $\Gamma_{\mathrm{E\times B}}$ which is driven by KPM has a more significant impact on particle transport. 80% of the total radial particle flux at the center of the pedestal is due to $\Gamma_{\mathrm{E\times B}}$. Experimental findings show that the density pump-out under RMP is highly correlated with the X-point deformation [58, 72]. Because KPM makes large displacement at the X-point, it may play an important role in the density pump-out, which is consistent with the tendency of experimental findings [48, 62]. Fig.3.8(b) shows the clearer correlation between the pedestal degradation and the radial transport; the radial heat and particle flux at $\psi_{\mathrm{N}} = 0.98$ of the LFS mid-plane start to increase with I_{RMP} while the gradients of both n_{e} and T pedestals decrease.

The above result suggests that the pedestal degradation by RMP is attributable not only to the formation of the stochastic layer but also to the

convective particle flux by the plasma response and other effects. This may support the experimental trend where the degradation of the density pedestal is much larger than that of the temperature pedestal.

The simulation results are compared with experimental data to validate the modeling of RMP. Because of the limitation in the diagnostics, only T_i and V_ϕ from CES measurement are mainly considered. The result is presented in Fig.3.9. Inverse gradient lengths of the temperature, L_Ti^{-1} and $L_{\mathrm{V}\phi}^{-1}$, at $\psi_\mathrm{N} = 0.98$ are plotted for various RMP coil currents. These are measured for the reference discharge (#18594). In the CES measurement (blue circle), the absolute values of both $\left|L_\mathrm{Ti}^{-1}\right|$ and $\left|L_{\mathrm{V}\phi}^{-1}\right|$ decrease with the external field strength. Although there is ambiguity in the experimental trend, $\left|L_\mathrm{Ti}^{-1}\right|$ and $\left|L_{\mathrm{V}\phi}^{-1}\right|$ seem to decrease by 30% and 38%, respectively, as I_RMP increases from 2 kA to 4 kA. In the simulation (orange triangle), $\left|L_\mathrm{Ti}^{-1}\right|$ shows similar behavior with the experiment. It varies from -0.64 to -0.44 (change of 31%) for the same change in I_RMP. We note the simulation result does not include the effect of harmonics with high n (≤ 14) and micro-instabilities on the RMP-driven transport. The assumption of $T_\mathrm{i} = T_\mathrm{e}$ is also used. Therefore, only the qualitative agreement between experiment and simulation can be evaluated. The change in $L_{\mathrm{V}\phi}^{-1}$ with I_RMP is small which does not follow the experimental trend where the V_ϕ pedestal is degraded with increasing I_RMP. It suggests that additional factors must be considered to explain the change of rotation.

3.3.2 NTV-driven transport

Toroidal symmetry breaking by RMP can induce NTV, which drives the radial particle transport and torque. Previous experimental studies confirmed the effect of NTV torque on the plasma rotation. However, particle transport by NTV

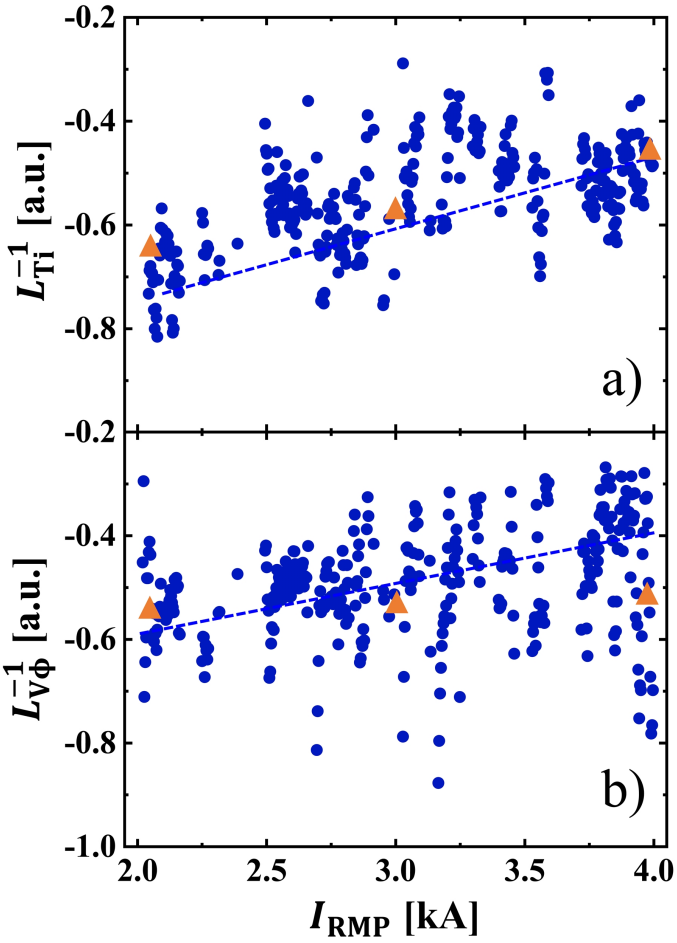

Figure 3.9: Experimental measurement for KSTAR shot #18594 of inverse gradient length of (a) ion temperature, L_{Ti}^{-1}, and (b) toroidal plasma rotation, $L_{\mathrm{V}\phi}^{-1}$, with increasing I_{RMP} are presented (blue dot). The blue dotted line corresponds to the trend line. Simulation results are plotted as orange triangles in each figure.

is still unclear. There was an attempt [73] to include NTV in the RMP analysis. It showed a considerable contribution of NTV to the n_e pedestal degradation by RMP but has limitations in that it uses heuristic NTV expressions and linear analysis. When RMP forms large magnetic islands, the system becomes nonlinear. In addition, the heuristic model is not proper to describe NTV with tearing structures. Because these islands are crucial in RMP physics, nonlinear study with a more accurate NTV calculation is needed to investigate NTV-driven transport.

In order to calculate the accurate NTV transport, Perturbed Equilibrium Non-ambipolar Transport (PENTRC) code is employed [74]. PENTRC requires the metrics of magnetic fields, the kinetic profiles, and the plasma displacement, ξ, of the equilibrium response by RMP. Here, the plasma information except ξ can be directly obtained from JOREK calculation. In general, ξ is challenging to define in nonlinear simulations where field reconnection occurs. Therefore, two assumptions are used to derive ξ. First, the temperature is assumed to be uniform on the field line because the parallel thermal diffusion is fast enough. Then, the perpendicular displacement can be defined as Eq.3.13.

$$\xi_\perp = \frac{\delta T}{\nabla T_{n=0,m=0}} \tag{3.13}$$

The application of Eq.3.13 on the JOREK calculation is shown in Fig.3.10. It shows that $\xi_\perp$ successfully catches the both even and odd components of $m = 8$ displacement (see the black dotted line), which comes from the kink and tearing responses, respectively. For the parallel displacement, I assume that the toroidal component of the first-order ideal force balances the perturbed plasma equilibrium. Based on this assumption, it is possible to calculate $\xi_\parallel$ from Eq.(16) of Ref. [75]. JOREK and PENTRC codes are coupled with the expression of

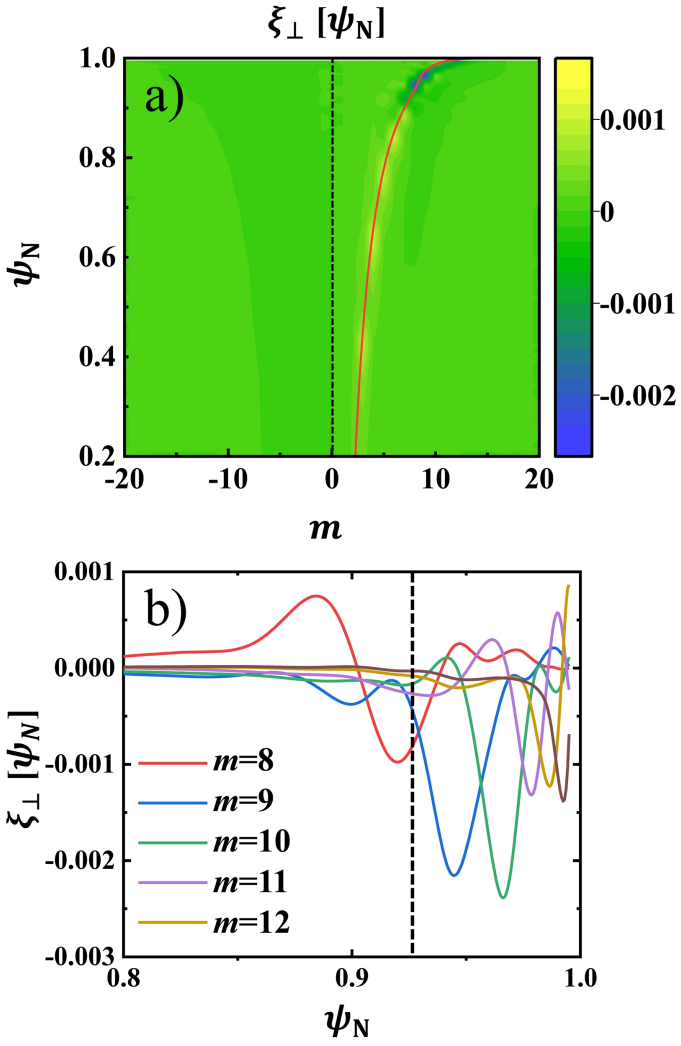

Figure 3.10: $n = 2$ components of the (a) perpendicular plasma displacement $\xi_\perp$ as functions of the poloidal mode number m and the normalized flux ψ_N, and (b) its radial mode structure are presented. In the figure (a), the resonant surfaces are plotted with the red line. In the figure (b), the black dotted line corresponds to the radial position of the $q = 4$ rational surface.

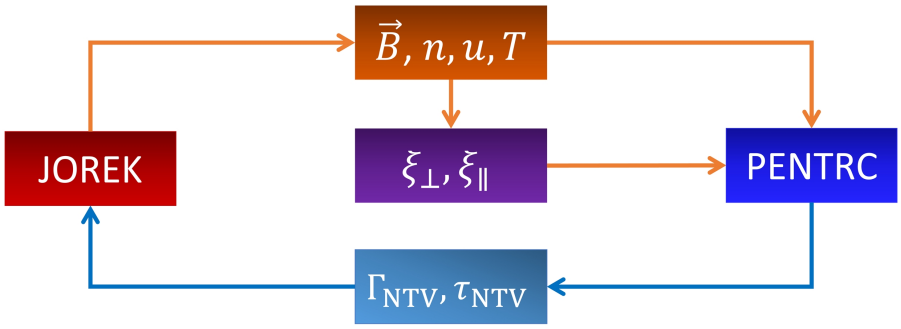

Figure 3.11: Schematic diagram for the code coupling between JOREK and PENTRC.

ξ. The schematic diagram for the code coupling is presented in Fig.3.11. By giving the information from JOREK to PENTRC, the NTV particle flux, Γ_{NTV}, and torque, τ_{NTV}, are calculated. After that, the NTV result is included in JOREK to update the calculation. This process is repeated until the equilibrium converges.

By this process, NTV is well reproduced by JOREK-PENTRC simulation. In Fig.3.12(a), it shows strongly edge localized structure under the presence of RMP. It turns out that NTV also degrades the pedestal. For example, Γ_{NTV} further reduces the n_{e} pedestal height by 10% as shown in Fig.3.12(b). Its effect is comparable to $\Gamma_{\mathrm{E\times B}}$ of kink response. Both Γ_{NTV} and $\Gamma_{\mathrm{E\times B}}$ degrade the pedestal, so overall density level, $\bar{n}_{\mathrm{e}}$, decreases by $6\times10^{17}\mathrm{m}^{-3}$. However, it is not consistent to the experimental value where $\bar{n}_{\mathrm{e}}$ is decreased by $2\times10^{18}\mathrm{m}^{-3}$. Therefore, KPM and NTV are not enough to fully explain the density pump-out in this study.

For the plasma rotation, NTV shows a significant effect. τ_{NTV} is $\sim$1.5 N·m which is the similar level as beam-driven torque ($\sim$3.3 N·m). Because the $L^{-1}_{\mathrm{V}\phi}$ is proportional to the net torque under the same momentum transport coefficient,

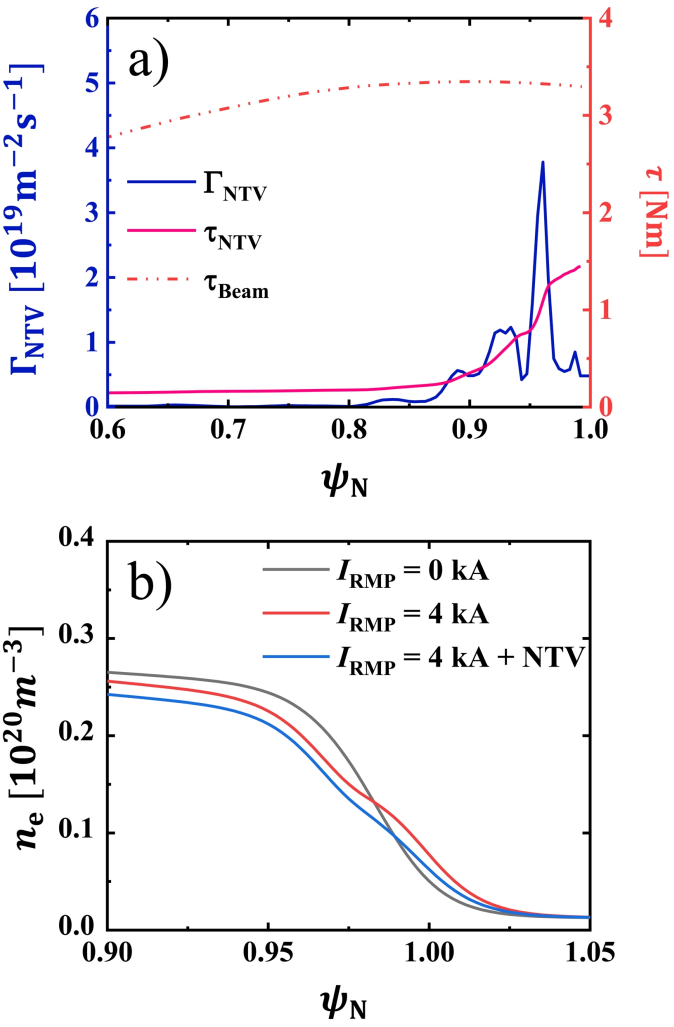

Figure 3.12: JOREK-PENTRC calculation results for (a) the radial NTV particle flux, Γ_{NTV}, the NTV torque, τ_{NTV}, and beam-driven torque, τ_{Beam}, are presented. In the figure (b), $n = 0$ profile degradation of n_{e} pedestal by RMP is shown, where NTV is included.

it is expected that τ_{NTV} degrades the V_ϕ pedestal ($\sim \psi_{\mathrm{N}} = 0.98$) roughly by 44%. This level is almost the same as the experimental observation ($\sim$ 38%), so NTV can be the main contributor to the V_ϕ degradation. Unfortunately, the momentum transport coefficient is unknown, and the momentum transport simulation with τ_{NTV} cannot be conducted. Therefore, it is difficult to discuss the exact change of V_ϕ in this study. In addition, further verification between JOREK-PENTRC and experimental result is required. They will be pursued as future work.

3.3.3 Limitation of applied modeling

The above modeling can quantitatively explain the change in the temperature and rotation by RMP. However, the degradation of the density pedestal cannot be fully explained in this simulation. Disagreement is also found in the stored energy, W_{MHD}. In the experiment, W_{MHD} is reduced by 8% as I_{RMP} increases from 2 kA to 4 kA. At the same time, W_{MHD} decrease by only 3% in the simulation, respectively.

The discrepancy between the experimental and the numerical result could result from the limitations of the simulation model. First, this study uses the simplified perpendicular diffusion profile and source models. Because the model cannot take into account the exact change of the core plasma transport, degradation of the plasma confinement with RMP can be smaller. Also, the profile stiffness has not been fully reflected in the simulation, which is a crucial characteristic of the core transport while pedestal changes. For better results, accurate diffusion coefficients and the source profiles based on the experimental data should be considered. In addition, the experimental trend considered in this study appears over 5 seconds in the experiment, where a significant change

in the background conditions (neutral pressure build-up, wall loading, wall temperature) can occur. These subtle changes can also contribute to the difference between the simulation and the experiment. In this respect, the simulation is expected to become more consistent with the experiment where the RMP current quickly increases while keeping the background conditions as constant as possible.

Second, the edge transport induced by RMP is also underestimated. Previous numerical studies revealed that radial transport at the pedestal region could be increased because of the destabilized edge localized ballooning modes [76,77]. The perturbed magnetic field structure can also induce transport by the magnetic flutter [78, 79] and polarization current [80]. Besides, we apply the Braginskii model to the parallel transport in the stochastic layer, which can underestimate the radial fluxes [81]. For example, the previous study reported that the Rechester-Rosenbluth diffusion model [82] better describes the transport in the stochastic layer [83]. Because these effects are not included in this work, the heat and particle flux may be undervalued. Overall, the pedestal degradation in the modeling can be smaller than that of the experimental measurement.

Furthermore, the fixed boundary model is used to calculate the RMP field penetration. This condition does not allow the modification of the magnetic perturbation at the boundary. Therefore, it may reduce the field amplification inside the plasma and modification of LCFS, which lessens the change of pedestal profile. In future work, these limitations in the transport and fixed boundary model will be resolved with JOREK-STAR WALL [84], which allows the variation of the perturbed field at the boundary.

Lastly, the destabilized micro-instabilities [85–87] by RMP can be a candidate. In particular, a recent global total-f gyrokinetic simulation by XGC [88]

addressed that RMP can enhance turbulence transport in the pedestal region. In this study, the RMP-driven potential structure and neoclassical effect affected the micro-instability. It provided evidence that such interaction increased the electron turbulence transport and contributed to the density-pump out. Because of the limitation of MHD modeling, the RMP-driven turbulence is expected to be a strong candidate to complement the explanation on the pump-out. Based on these modeling results, the main candidates to explain the pedestal degradation by RMP is summarized in Table 3.1.

Table 3.1: Contributors to the pedestal degradation by RMP

Channel	Expected main contributor
Temperature	- Conductive heat transport through chaotic layer - Turbulence thermal transport
Density	- Turbulence particle transport - Convective particle transport through kink layer - Magnetic flutter
Rotation	- NTV torque

Chapter 4

RMP-driven ELM crash suppression

The initial hypothesis of the RMP-driven ELM suppression mechanism relies on the linear stabilization of PBM by RMP. Therefore, the plasma condition which can maximize the external field penetration, such as $V_{\perp,\mathrm{e}} \approx 0$, will be favorable in this respect. However, this hypothesis has difficulties in explaining the occurrence of PBM-like coherent modes during the suppression phase [24]. For example, Fig.4.1 shows the edge localized filament structure when the suppression is achieved. In addition, the experimental scan suggested that $V_{\theta,\mathrm{E}} \approx 0$ is more important to ELM control than $V_{\perp,\mathrm{e}} \approx 0$ near the pedestal top [89]. There was a study on the effect of $V_{\theta,\mathrm{E}} \approx 0$ in terms of field penetration [90], but the reason for the experimental result is still unclear. Because of these limitations, additional effects are needed to fully explain the ELM crash suppression.

Several studies have focused on the direct coupling between RMPs and ELMs to explain the experimental trend. The linear analysis found that the

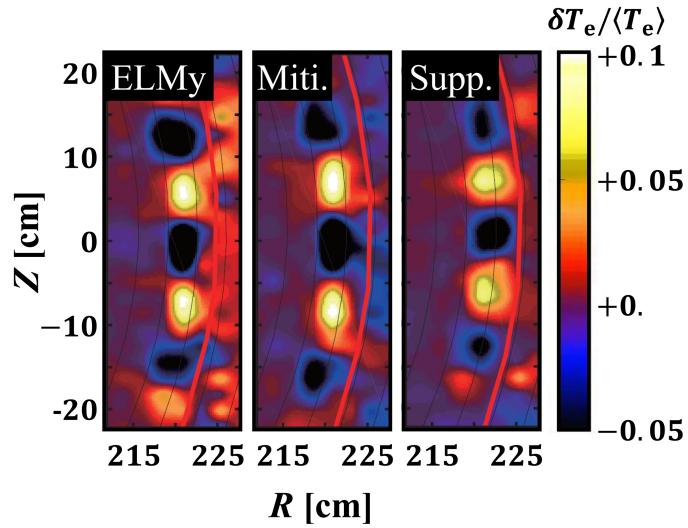

Figure 4.1: Experimental observation of Edge localised mode structure in ELMy, mitigation, and suppression phase in KSTAR discharge [7].

properties and stability of PBM change with 3D-field modulation by RMPs [76, 77]. A nonlinear MHD simulation showed that PBM could be saturated by this mode coupling effect [91–93]. Furthermore, the experimental observation reported the bifurcation of mode frequency of PBM by RMP [25], and it also supports the importance of mode coupling on the ELM suppression. However, the exact role of mode coupling is unknown, and further study with nonlinear simulation is needed.

4.1 Numerical setup for analysis

4.1.1 Natural ELM simulation

In order to study the ELM suppression by RMPs, it is essential to check if PBMs occur also without RMP to be consistent with the experimental data. For this purpose, the linear PBM stability of the initial phase is checked.

In our reference time slice (6.45 s), when the effect of RMP was minimal or not yet effective, n of the most unstable PBM was 11 ± 1 in the linear phase from ECEI diagnostics. The temperature fluctuation, δT_{e}, for the $n = 12$ PBM inside separatrix with $\Delta t \sim 60\mu$s ($= 120\tau_{\mathrm{A}}$) is presented in Fig.4.2(a), where $\langle .. \rangle_t$ means time averaged value. In the measurement, the mode structure was poloidally rotating in the ion-diamagnetic direction ($-Z$ direction at LFS) with $V_{\theta,\mathrm{mode,exp}} \sim 2.9$ km/s in the lab frame.

To calculate the linear behavior of PBM, a single harmonic with $n = 12$ is launched on the kinetic equilibrium with a small amplitude at the numerical noise level ($\sim 10^{-27}$) in the JOREK unit. Then, the linear phase of PBM is modeled. Its linear growth rate is $\gamma\tau_{\mathrm{A}} \sim 0.054$. The resulting δT_{e} for $n = 12$ PBM at LFS in the lab frame corresponds to Fig.4.2(b). Here, δT_{e} is taken near the end of the linear phase with $\Delta t \sim 55\mu$s ($= 110\tau_{\mathrm{A}}$), and $\langle T_{\mathrm{e}} \rangle_t$ is derived from its background ($n = 0$) value. In the figure, the $n = 12$ mode structure rotates in the ion-diamagnetic direction at about $V_{\theta,\mathrm{mode}} \sim 3.2$ km/s, which shows good agreement with the ECEI measurement (~ 2.9 km/s). It is noteworthy that $V_{\theta,\mathrm{mode}}$ is similar to $V_{\theta,\mathrm{E}}(\sim 2.8$ km/s) at the mode location. In our case, the poloidal $E \times B$ velocity $V_{\theta,\mathrm{E}} = \hat{e}_\theta \cdot \vec{V}_{\mathrm{E}}$ at the pedestal is in the ion-diamagnetic direction due to large V_ϕ [55], and therefore modes rotate in the clockwise direction. This similarity between $V_{\theta,\mathrm{mode}}$ and $V_{\theta,\mathrm{E}}$ is also consistent with the previous studies [55, 94].

As ELM is not a single mode event but a nonlinear MHD phenomenon, the mode coupling should be considered in the modeling. Therefore, the nonlinear simulation including multi harmonics is conducted for the next step. Although $n = 12$ is the most unstable mode, harmonics of $n = 2$, 4, 6, 8, 10, 12, and 14 have been considered within the limits of the computational resources. The

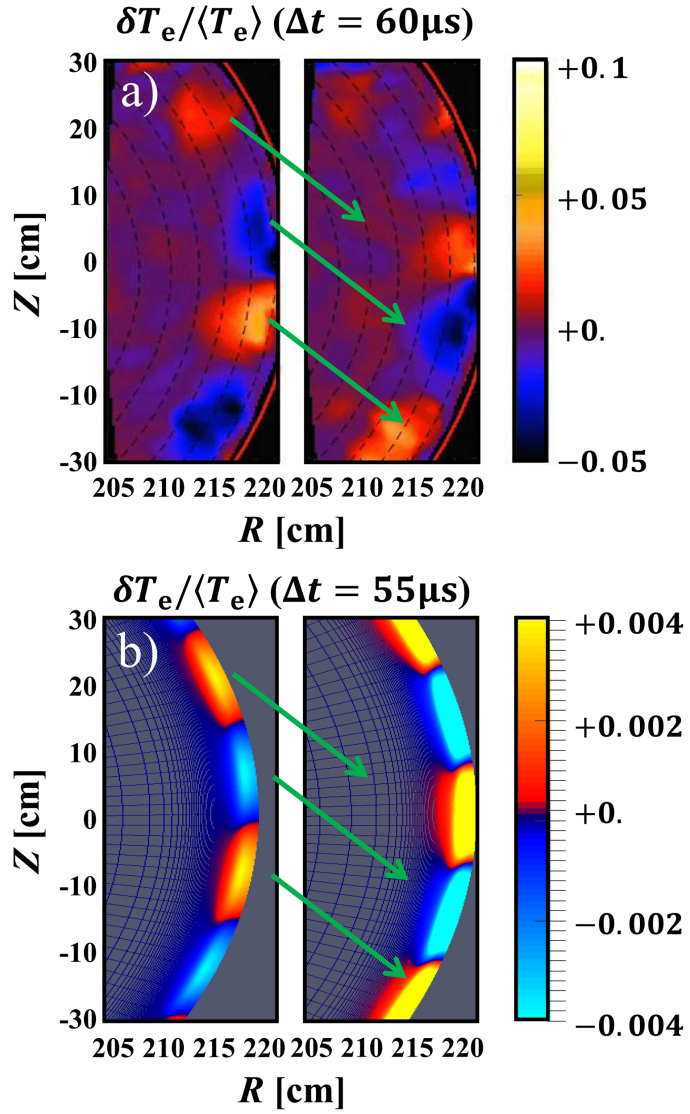

Figure 4.2: (a) 2D measurement of electron temperature fluctuation in $R - Z$ space from ECEI diagnostics ($n = 12$) in the LFS region at consecutive times slices of $\Delta t = 60\mu$s. (b) Simulation result of electron temperature fluctuation at two different time slices with $\Delta t = 55\mu$s near the onset of mode crash.

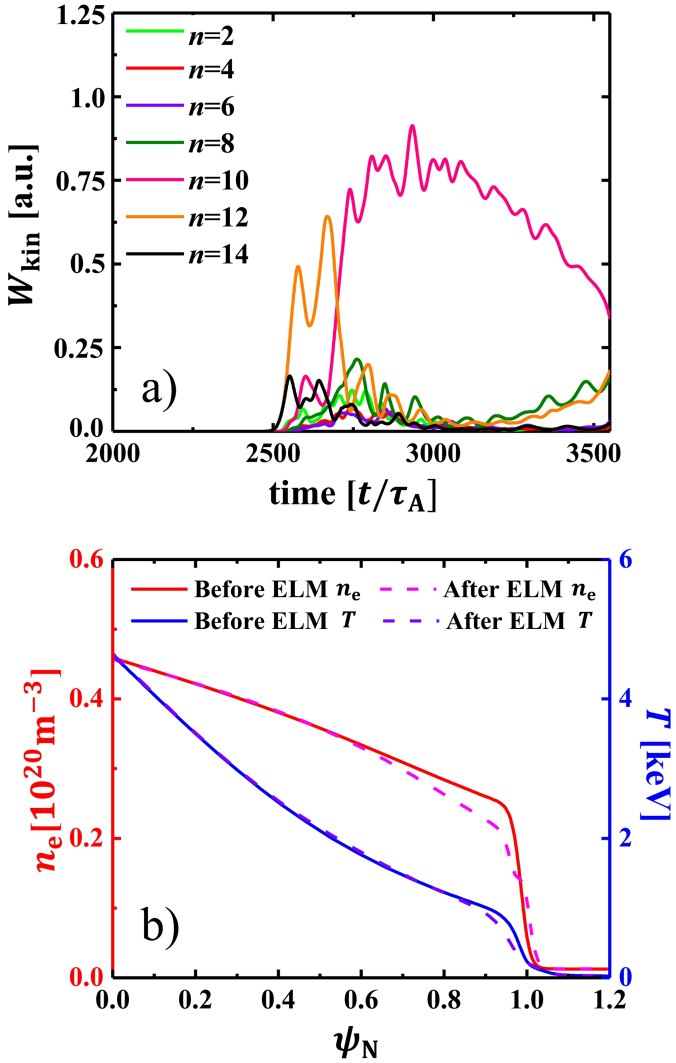

Figure 4.3: (a) Time evolution of the toroidal harmonics of the kinetic energy for $n = 2 \sim 14$. (b) Comparison of n_e and T_e before the onset of ELM ($\sim 2500\tau_A$) and after the crash ($\sim 3500\tau_A$). They show the nonlinear phase of natural PBM without RMP.

results for the perturbed kinetic energy $W_{\rm kin} = \int \rho \left|\nabla_\perp u\right|^2 dV/2$ of PBM in the nonlinear phase are shown in Fig.4.3(a). Here, $n = 12$ is the fastest growing mode to enter the nonlinear phase first. Then, other modes including $n = 10$ are driven by mode coupling in the nonlinear phase [95], which results in a bursty MHD behavior with mode crashes. For example, the amplitude of $n = 10$ mode increases during the $n = 12$ mode crash. The $n = 10$ mode starts to crash $700\tau_{\rm A}$ after the crash of the $n = 12$ mode. During the mode crash, the nonlinear Maxwell stress induces the strong shear of the plasma filaments. As a consequence, thermal energy and particles are expelled across the separatrix, resulting in flows and shearing-off of the large heat flux across SOL [55, 96].

Fig.4.3(b) shows the change of density and temperature pedestal at $\sim 3500\tau_{\rm A}$ from the simulation. Both pedestals are collapsed as the PBM crash occurs. For example, heights of density and temperature pedestal decreased by 26% and 21%, respectively. The stored energy also decreased by $\Delta W_{\rm ELM,Sim} \approx 8.1$ kJ, which is close to the experimental value $\Delta W_{\rm ELM,Exp} \approx 7(\pm 2)$ kJ. Because the magnitude of the crash increases with the mode amplitude in the nonlinear phase, the ELM size also increases with $W_{\rm kin}$. Therefore, the largest perturbed kinetic energy during the nonlinear phase, $W_{\rm kin,max}$, is used to estimate the size of PBM or ELM in the later sections.

4.1.2 Numerical modeling of RMP and PBM

PBMs with $n \leq 14$ are included in the simulation to study the effect of RMP-induced plasma response on PBM. Note that $n > 14$ modes are also linearly unstable, and the $n = 12$ mode is the most unstable. Because the growth rate of $n = 10$ is similar to that of $n = 12$ as low n modes are dominant in the nonlinear phase, it is reasonable to exclude $n > 14$ modes to meet the limit of

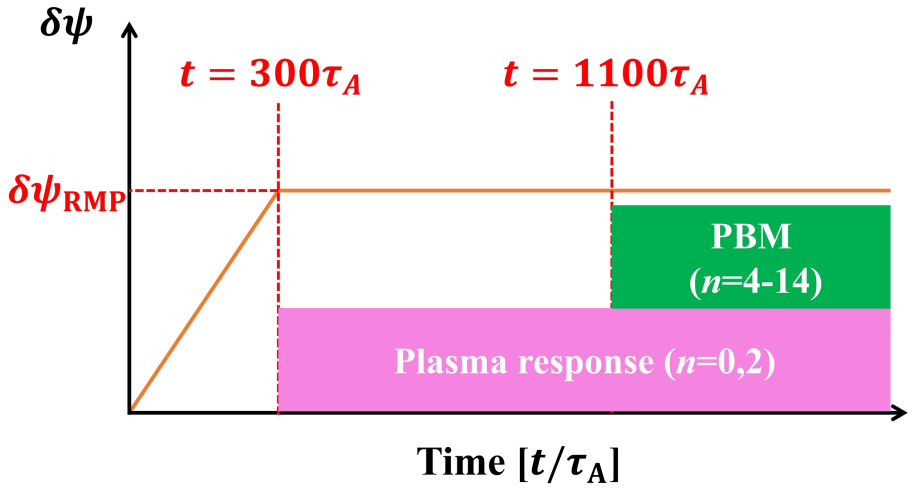

Figure 4.4: Schematic diagram for the numerical modeling of RMP and PBM in JOREK simulation.

our computing resources. Also, previous numerical modeling [92] revealed that the $n = 2$ structure induced by RMP suppresses the growth of odd modes and only even modes play a dominant role in the nonlinear phase when RMP is applied. Therefore, $n = 2$, 4, 6, 8, 10, 12, and 14 modes are considered in this study. Nevertheless, one of the important limitations of this study is that only a limited number of even modes are considered.

To study the direct effect of RMP on PBM, We first calculate the evolution of the $n = 0$ and 2 modes in the presence of RMP for $t \sim 800\tau_A$ with the same method described in Chapter.3. Then, $n = 4$, 6, 8, 10, 12, and 14 are added with an initial amplitude imposed by the coupling with $n = 2$ to see how PBM interacts with RMP. We note that PBM is the intrinsic component where $n > 2$ rather than $n = 2$ components according to RMP application. The schematic diagram of the RMP modeling process is presented in Fig.4.4. In this way, the interaction between RMP and PBM is evaluated self-consistently.

4.2 ELM crash suppression

4.2.1 PBM suppression

The simulation results for the case with I_{RMP} of 1 kA, 2 kA, 3 kA, and 4 kA are presented in Fig.4.5. The orange dotted line in the figure indicates $W_{\mathrm{kin,max}}$ in the natural PBM simulation. For $I_{\mathrm{RMP}} \leq 2$ kA, PBM of $n = 6$ and 8 exponentially grow in the linear phase and show bursty behaviors at the nonlinear phase. The overall mode amplitude during the nonlinear phase slightly decreases by 30% compared to the Natural ELM case.

When RMP of $I_{\mathrm{RMP}} = 3$ kA is applied, the overall mode amplitude during the nonlinear phase decreases by 75%. The dominant mode in the linear phase changes to $n = 4 - 6$. This is due to the interactions between the $n = 2$ RMP-driven mode and PBMs. It is consistent with the report that the modified field structure induced by RMP changes the dominant mode number to lower n [77]. However, there is still a crash in the nonlinear phase, and filaments are expelled similarly as in the natural PBM case, but with much smaller amplitudes. Therefore, PBMs are mitigated in this case.

On the other hand, PBMs are suppressed with $I_{\mathrm{RMP}} = 4$ kA. The most unstable mode changes to $n = 4$ and shows bursts of very low amplitude only. After that, all modes are saturated and remain stationary without any bursty behavior [97]. Their saturated value is similar to the initial amplitude imposed by the coupling with $n = 2$. It is noteworthy that ELMs are suppressed in the experiment with $I_{\mathrm{RMP}} \sim 3.7$ kA, which agrees fairly well with our modeling results (~ 4 kA). This result shows better agreement than Ref. [92], where the mode suppression was achieved with the perturbed field, 1.5 times larger than the experimental value.

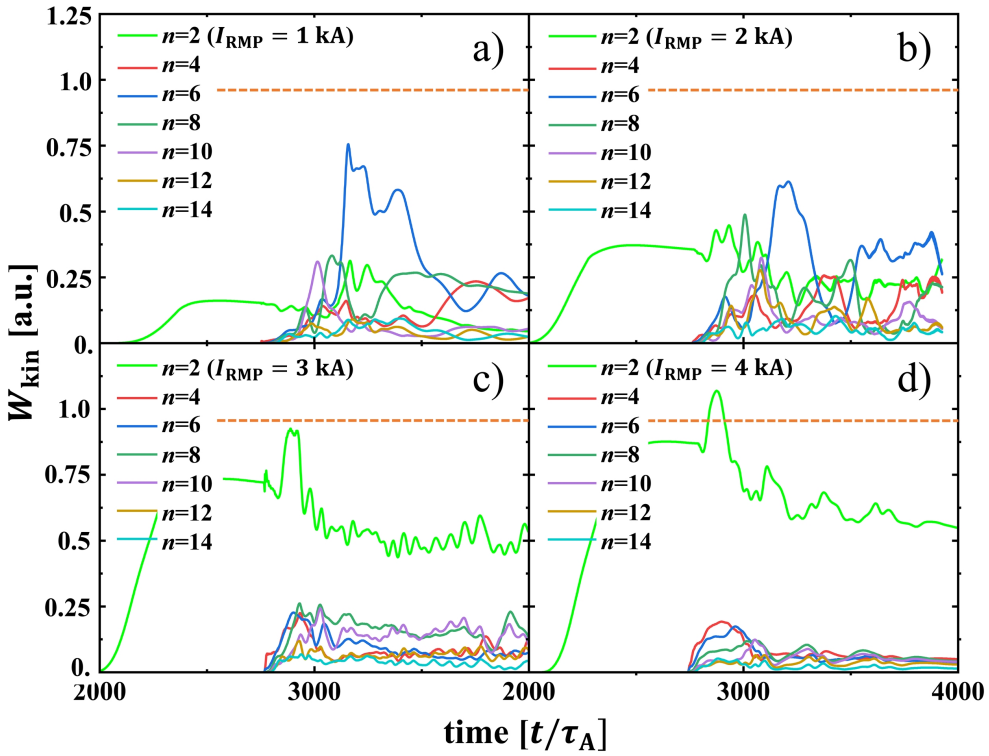

Figure 4.5: Time evolution of the toroidal harmonics of the kinetic energy for $n = 2 \sim 14$ is presented. Each figure corresponds to the case of PBM with I_{RMP} equals to (a) 1 kA, (b) 2 kA, (c) 3 kA, and (d) 4 kA. Units are arbitrary, but the normalization is the same in all cases. The orange dotted line represents the maximum W_{kin} in the natural ELM simulation. Here, $n = 2$ mode is the RMP-induced mode.

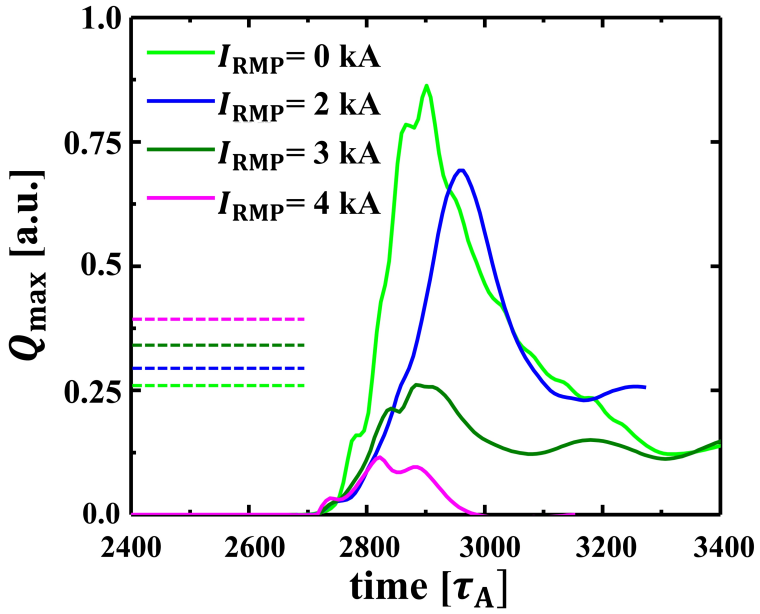

Figure 4.6: Time evolution of the ELMy heat flux (solid line) and background heat flux (dotted line) on the lower divertor of the LFS for various I_{RMP} are presented. It shows that ELMy heat flux decreases with I_{RMP} while background heat flux increases.

4.2.2 Change in divertor heat flux

The effect of RMP on the heat flux at the divertor during ELMs is also investigated. Fig.4.6 shows the instantaneous ELMy peak heat flux, $Q_{\mathrm{ELM,max}}$ ($= Q_{\mathrm{max}} - Q_{\mathrm{BG}}$) (solid line) and background heat flux, Q_{BG} (dotted line) on the lower-outer divertor plate during the mode crashes. In Fig.4.6, Q_{BG} has been removed from the actual peak heat flux, Q_{max}, to compare $Q_{\mathrm{ELM,max}}$. Here, the time axis for each case is shifted to the left by $0\tau_{\mathrm{A}}$(0 kA), $150\tau_{\mathrm{A}}$(2 kA), $70\tau_{\mathrm{A}}$(3 kA), and $30\tau_{\mathrm{A}}$(4 kA), respectively, to make the comparison easier. When $I_{\mathrm{RMP}} = 2$ kA is applied, $Q_{\mathrm{ELM,max}}$ decreases by 28% from that of the

natural PBM case. For $I_{\mathrm{RMP}} > 2$ kA, $Q_{\mathrm{ELM,max}}$ starts to change drastically and eventually decreases by 88% at $I_{\mathrm{RMP}} = 4$ kA, where PBMs are suppressed. Because $Q_{\mathrm{ELM,max}}$ for $I_{\mathrm{RMP}} = 4$ kA is lower than 35% of the background heat flux, it is negligible. Therefore, we can say that suppression of PBM results in a significant reduction in the heat flux that agrees with the experiments [98, 99].

The background heat flux increases by 50% from the reference value at $I_{\mathrm{RMP}} = 4$ kA. It is mainly due to the increased radial transport from the core to SOL, which is consistent with experimental trends [99–101]. Although it is not shown here, the striation pattern of the divertor heat flux is not apparent in our case as tangles induced by RMP [52] are not large enough to affect the heat flux. Detailed analysis of the effect of tangles in divertor heat flux of KSTAR will be pursued as future work. Note that there is a lack of diagnostics, and the KSTAR divertor configuration is not considered accurately in the modeling. As a consequence, a direct comparison of the simulation with the measurement of divertor heat flux is difficult, and it will also be addressed in future works.

The ELMy heat flux during the ELM mitigation is usually smaller [100] than that of natural ELM in the experiments, which is consistent with the above results. However, the simulation result shows the possibility of increased ELMy heat flux during the mitigation phase. It is related to the fact that the divertor heat flux depends not only on the amplitude of the mode crash but also n of the most unstable PBM. For example, the peak ELMy divertor heat flux tends to increase as the dominant n becomes lower [102]. Because the amplitude and the dominant n of PBM decrease simultaneously in the ELM mitigation case, the non-monotonic tendency of ELMy heat flux may be observed in the mitigation case. Also, the stochastic field and the tangle structure caused by RMP change the divertor heat flux. However, they cannot be properly considered in this

modeling because accurate divertor physics such as neutral recycling, source, and diffusion profiles are not included. Further studies will be required for improving the modeling of the divertor heat flux.

4.3 RMP and PBM coupling

Suppression of PBM with the perturbed field could be related to the degraded mean pedestal, which is the source of PBM. It could also result from the increased mode coupling of PBM ($n > 2$) with RMP-induced plasma response ($n = 2$), which has been found in previous studies [91, 92]. To find the main factor of mode suppression, PBM stability is investigated with the degraded mean density and temperature profile, while mode coupling of PBM with RMP is excluded. This is done as the simulation with a pressure gradient and current density modified to the same level as in the ELM suppression case ($I_{\mathrm{RMP}} = 4$ kA), but without applying RMPs. As shown in Fig.4.7(a), the linear growth rate of PBM decreases more than 60% for all n as compared to the case without pedestal degradation. However, PBMs are still non-linearly unstable, and a significant mode crash occurs despite small growth rates. In Fig.4.7(b), mode saturation is possible only when mode coupling is included. This indicates that the mode coupling has a dominant effect on the ELM suppression of our case rather than the reduced destabilizing source owing to the pedestal degradation.

4.3.1 Effect on the pedestal transport

It turns out that the mode coupling can change the magnitude of the field penetration by RMP. Fig.4.8(a) shows δB_{r} and $\delta B'_{\mathrm{r}}$ ($= \partial \delta B_{\mathrm{r}} / \partial \psi_{\mathrm{N}}$) of the $q = 4.5$ rational surface on the center of the pedestal ($\psi_{\mathrm{N}} \sim 0.98$). Here, δB_{r} and $\delta B'_{\mathrm{r}}$ are the radial perturbed field strength and its radial gradient of $[m, n] = [9, 2]$

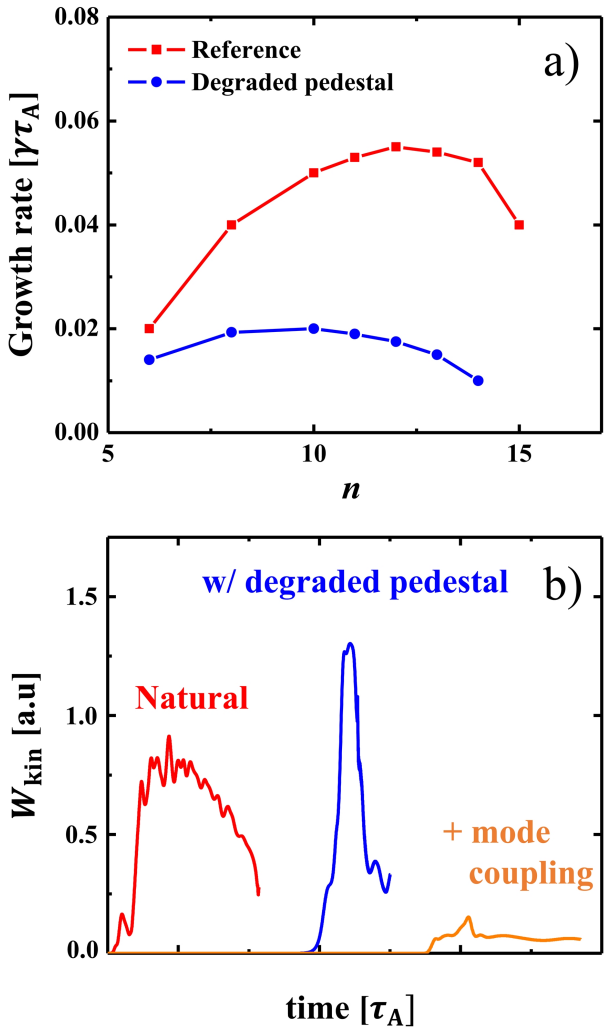

Figure 4.7: (a) Spectrum of the linear growth rate. The red line and blue line correspond to the growth rate of PBM for reference equilibrium and for that with degraded pedestal induced by RMP, respectively. (b) Nonlinear evolution of W_{kin} of $n = 10$ component for the natural PBM (red line), for PBM with degraded pedestal (blue line), and for PBM with mode coupling including RMP (orange line).

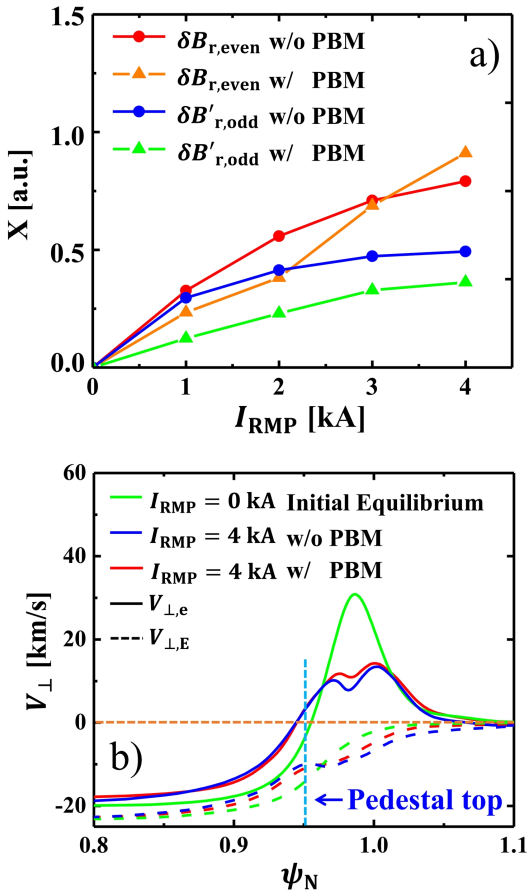

Figure 4.8: a) $\delta B_{\mathrm{r,even}}$ and $\delta B'_{\mathrm{r,odd}}$ of $[m, n]$=[9,2] on the $q = 4.5$ rational surface for various I_{RMP}. The orange line and red line correspond to the radial perturbed field strength of even parity, $\delta B_{\mathrm{r,even}}$, with and without mode coupling between PBMs, respectively. The green line and blue line represent the radial gradient of the perturbed field strength of odd parity, $\delta B'_{\mathrm{r,odd}}$, with and without PBM, respectively. (b) The radial profile of the $E \times B$ flow, $V_{\perp,\mathrm{E}}$ (dotted line), and electron flow, $V_{\perp,\mathrm{e}}$ (solid line). The green color corresponds to the initial equilibrium case. The red and blue colors represent the cases with and without PBM, respectively. The orange dotted line corresponds to $V_\perp = 0$.

at $t = 3800\tau_{\mathrm{A}}$, respectively. The even parity $\delta B_{\mathrm{r,even}}$ represents the size of the magnetic island, and the odd parity $\delta B'_{\mathrm{r,odd}}$ means the strength of the kink-peeling response. In the figure, $\delta B'_{\mathrm{r,odd}}$ with the mode coupling between PBM is smaller than the case without it for all I_{RMP}. This is consistent with the decrease in the energy of $n = 2$ mode when PBM are included (see Fig.4.5). This may support that the energy exchange between the $n = 2$ RMP-driven mode and PBM is mediated by the $n = 2$ kink-peeling component.

On the other hand, $\delta B_{\mathrm{r,even}}$ shows a different behavior. When $I_{\mathrm{RMP}} < 3$ kA, $\delta B_{\mathrm{r,even}}$ has a similar tendency as $\delta B'_{\mathrm{r,odd}}$. On the other hand, for $I_{\mathrm{RMP}} > 3$ kA, $\delta B_{\mathrm{r,even}}$ with PBM becomes larger than the case without it. Once again, ELM suppression is achieved with $I_{\mathrm{RMP}} \sim 4$ kA. To understand the steep increase in $\delta B_{\mathrm{r,even}}$ at $I_{\mathrm{RMP}} \sim 4$ kA, the change in the plasma flow is investigated. Fig.4.8(b) shows the perpendicular $E \times B$ flow, $V_{\perp,\mathrm{E\times B}}$, and the electron flow, $V_{\perp,\mathrm{e}}$, for the cases with and without PBM. In the figure, there is no significant flow reduction even with PBM. Rather, the inclusion of PBM increases $V_{\perp,\mathrm{e}}$ at the pedestal center, which can reduce the field penetration. Therefore, the increase in $\delta B_{\mathrm{r,even}}$ by PBM can be more correlated with the mode interaction between the RMP-driven mode and PBM rather than with the influence of the flow.

The increased $\delta B_{\mathrm{r,even}}$ and the island size can further reduce the pedestal gradient. As shown in Fig.4.9, the pedestal gradient further decreases by 8% when the interaction of PBMs and RMP is included. Therefore, the mode coupling effect can also help ELM suppression by enhancing the magnetic island and degrading the pedestal. As the interaction between the magnetic island and PBMs turns out to be important, future work may be needed to consider the plasma resistivity, which should affect magnetic islands and field penetration

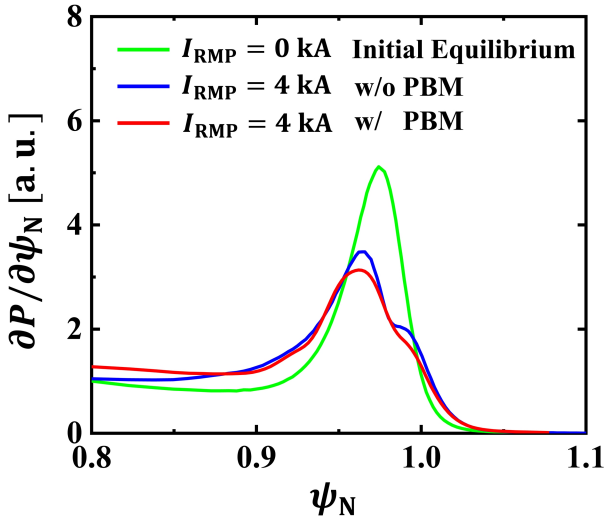

Figure 4.9: The radial profile of the pressure gradient $\partial P/\partial \psi_{\mathrm{N}}$. The green color corresponds to the initial equilibrium case. The red and blue colors represent the cases with and without mode coupling effect, respectively.

more strongly than the mode coupling.

4.3.2 Effect on the spectral transfer

Evidence of strong mode coupling between PBMs ($n > 2$) and RMP ($n = 2$) during the mode suppression can be also found in Fig.4.5(d). In the early phase, $n = 4$ mode rapidly grows and reaches $W_{\mathrm{kin}} \approx 0.18$. Then, $n = 2$ mode induced by RMP starts to increase and followed by a decrease of $n = 4$ mode. After that, $n = 2$ mode decreases while $n = 6$ mode starts to grow. Similar patterns are repeated afterward.

Such interactions can be quantified as $C[n_1, n_2]$, which is the correlation coefficient for mode amplitude $\delta\phi^2(t)$ of n_1 and n_2 harmonics. The result is presented in Fig.4.10. $C[n_1, n_2]$ is calculated during the nonlinear phase, where

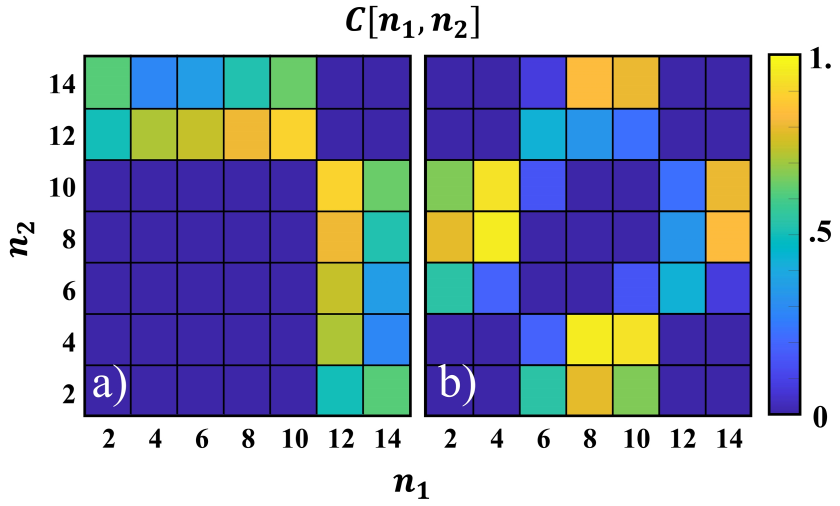

Figure 4.10: The time correlation coefficient of different harmonics during the nonlinear phase for a) the natural ELM case and b) the suppression case ($I_{\mathrm{RMP}} = 4$ kA).

mode crash occurs. In the natural ELM case, the interactions between harmonics are mainly done by $n = 10 - 14$, which is the most unstable mode. Because unstable modes have a large amplitude, they drive the overall mode couplings. However, in the case of ELM suppression ($I_{\mathrm{RMP}} = 4$ kA), the mode interactions appear over a wide range of n. This result addresses that energy exchanges between PBMs can be enhanced by $n = 2$ RMP-driven mode. Here, $n = 2$ mode helps PBMs to share energies among themselves by extracting the energy of the rapidly growing mode and by spreading it to others.

For additional analysis of the mode coupling, bi-spectral analysis is conducted on the perturbed harmonics. The bi-spectral coefficient for the variable X, B_{X}, is defined as Eq.4.1,

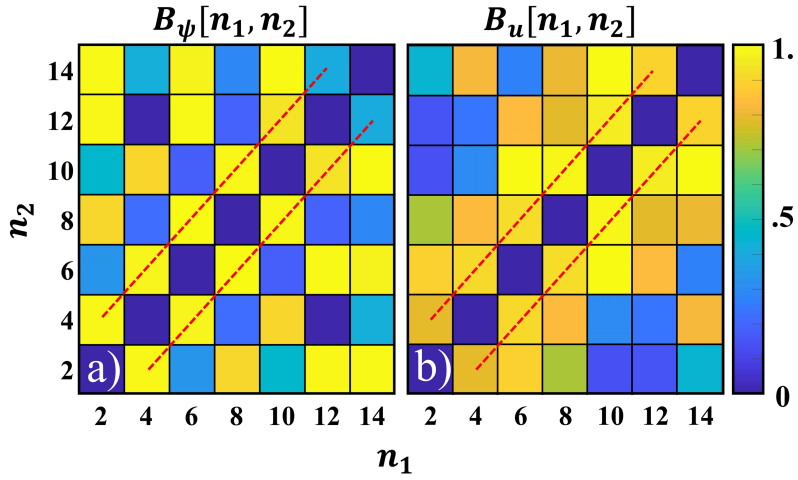

Figure 4.11: The bi-spectral coefficient of different harmonics at $q = 4.5$ rational surface for a) the perturbed poloidal flux and b) the potential with $I_{\mathrm{RMP}} = 4$ kA (ELM suppression case). The $t = 2950\tau_{\mathrm{A}}$ is selected as the target time slice. The red dotted line represents $|n_2 - n_1| = 2$.

$$B_{\mathrm{X}}[n_1, n_2] = \frac{X^*_{n2} X_{(n2-n1)} X_{n1}}{|X^*_{n2}| \left| X_{(n2-n1)} X_{n1} \right|} \tag{4.1}$$

where (*) denotes the conjugate operator. B_{X} represents the nonlinear coupling of mode component in a specific region for a single time slice while $C[n_1, n_2]$ can capture the global interaction over time. So B_{X} is suitable for detailed analysis. The bi-spectral coefficient for the perturbed poloidal flux B_ψ and the potential B_{u} with $I_{\mathrm{RMP}} = 4$ kA is calculated at the $q = 4.5$ rational surface at the center of the pedestal. $t = 2950\tau_{\mathrm{A}}$ is selected as the target time. We note that $\delta\psi$ and δu of the tearing component have the even and the odd parity, respectively. Therefore, B_ψ is more related to the coupling between the tearing modes. On the other hand, B_{u} represents the interactions of kink and ballooning modes. The bi-spectral analysis result is shown in Fig.4.11. Once

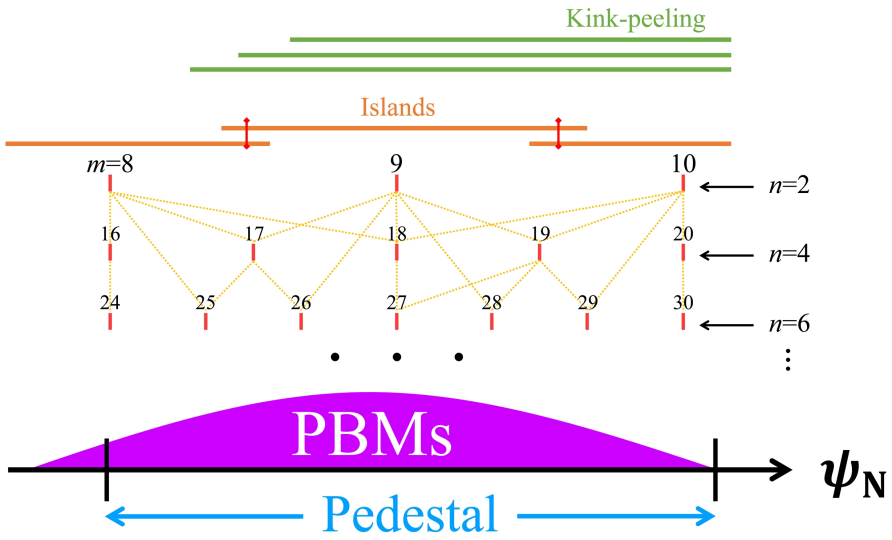

Figure 4.12: The schematic diagram of the interaction between different $[m, n]$ components at the pedestal. The green and orange lines correspond to the radial width of kink and island structure driven by $n = 2$ RMP, respectively.

again, it is confirmed that mode coupling has been largely enhanced in the ELM suppression case. In particular, the mode coupling occurs largely over $|n_1 - n_2| = 2$. It addresses that $n = 2$ mode is a bridge that mediates the interactions between all harmonics. Besides, the norm of B_ψ and B_u is 3.59 and 3.07, respectively. Because they have similar size, both tearing and twisting parity modes play an important role in the mode coupling.

The $n = 2$ RMP-driven mode governs interactions between RMP and PBM, and both kink and tearing components participate at the same time. From these findings, several requirements for ELM suppression can be suggested. In order for $[m_1, 2]$ mode to interact with $[m_2, n]$, $[m_2 - m_1, n - 2]$ mode has to be participated. For their interaction, the spatial overlapping of $[m_1, 2]$ and $[m_2 - m_1, n - 2]$ is essential. The schematic diagram of these interactions is presented

in Fig.4.12. As shown in the figure, $n = 2$ components can interfere with the $n > 2$ modes through the interaction with other overlapping modes. We note that most components of unstable PBM generally stay in the pedestal region. Here, $n = 2$ components should radially cover PBM to mediate their energy and suppress them. Furthermore, all $n = 2$ parity modes have to overlap each other to enhance the coupling with low to high n modes. The kink components have a large non-resonant part, and their spatial coupling can easily occur. However, its structure is localized to LCFS, so it is not enough to cover the region near the pedestal top to mediate nonlinear interaction. On the other hand, the tearing components have a small non-resonant part, and it is not sufficient for the island to overlap. Nevertheless, its resonant part can form over the wide radial range. Therefore, if the width of the magnetic island is large enough for island overlap, they can support mode interaction near the top of the pedestal. From this point of view, three requirements can be addressed. They are 1) large kink-peeling response, 2) $n = n_{\mathrm{RMP}}$ rational surface near the pedestal top (or slightly inner) and center, and 3) magnetic island overlap. If these conditions are satisfied, the kink and tearing components can mediate the interactions between PBMs in the entire pedestal region and support the ELM suppression.

The reference plasma of this study has $q = 8/2$ and $q = 9/2$ rational surface at the pedestal top and the center, respectively. A large KPM response also occurs. In addition, the effect of the island overlap on the mode coupling is tested. Chiricov parameter $S_{(\mathrm{m1,m2})}$ is defined as Eq.4.2 to quantify the overlap between $[m_1, 2]$ and $q = [m_2, 2]$ islands,

$$S[m_1, m_2] = \left| \frac{w_{\mathrm{m1}} + w_{\mathrm{m2}}}{\psi_{\mathrm{N,m1}} - \psi_{\mathrm{N,m2}}} \right|, \tag{4.2}$$

where $\psi_{\mathrm{N,m}}$ and w_{m} are the radial location and half-width of $[m, 2]$ island,

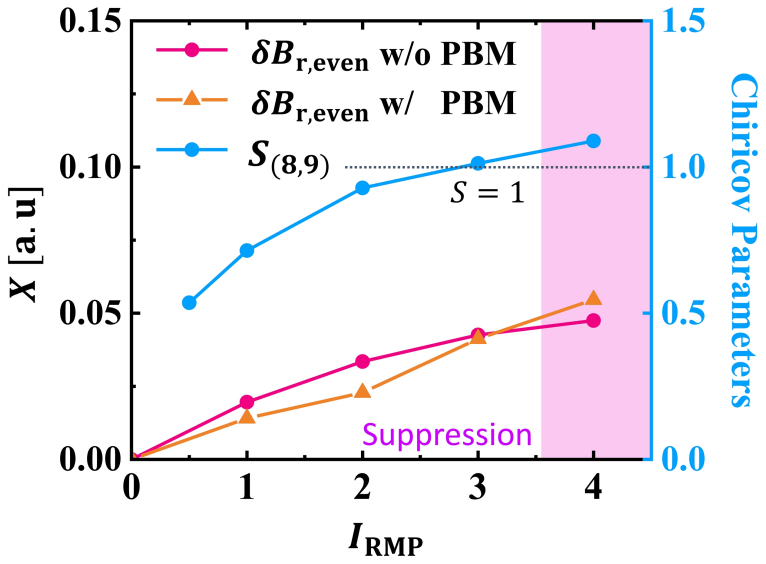

Figure 4.13: $\delta B_{\mathrm{r,even}}$ of $[m,n]$=[9,2] on the $q = 4.5$ rational surface for various I_{RMP}. The orange line and red line correspond to the radial perturbed field strength of even parity, $\delta B_{\mathrm{r,even}}$, with and without mode coupling between PBMs, respectively. The blue line represents the chiricov parameter for [8,2] and [9,2] magnetic islands.

respectively. The w_{m} is derived from the approximate expression, Eq.4.3, with minor radius r, total poloidal flux ψ_{a} and poloidal mode number m.

$$w_{\mathrm{m,n}} = \frac{2RB_\theta}{\psi_{\mathrm{a}}} \sqrt{\left| \frac{rqB_{\mathrm{r,even,mn}}}{m\partial q/\partial r B_\theta} \right|} \tag{4.3}$$

Here, the island overlap occurs if $S_{(\mathrm{m1,m2})} > 1$. $S_{(8,9)}$ with varying I_{RMP} is calculated as shown in Fig.4.13. $\delta B_{\mathrm{r,even}}$ at $q = 9/2$ of Fig.4.8 is also presented in the same figure. $\delta B_{\mathrm{r,even}}$ with PBM starts to rapidly increase near $S_{(\mathrm{m1,m2})} \sim 1$. Because the island overlap occurs at this point, it strengthens the interpretation that the increase in $\delta B_{\mathrm{r,even}}$ by PBM is the consequence of the mode interaction. We note that $S_{(9,10)}$ is already larger than unity for $I_{\mathrm{RMP}} > 1$ kA. When $S_{(\mathrm{m1,m2})}$ exceeds unity at $I_{\mathrm{RMP}} = 4$ kA, the ELM suppression is achieved. Because the mode coupling largely increases for $S_{(\mathrm{m1,m2})} > 1$, the island overlap near the pedestal top can be an important condition for the mode suppression in terms of interaction between RMP and PBM. Interestingly, pedestal degradation requires large stochasticity, but this result suggests that weak stochasticity ($S_{(8,9)} \gtrsim 1$) may be sufficient for ELM suppression.

Another interesting feature of the ELM suppression case is a significant change in the vorticity profile $U(= \nabla^2 u)$. It is found that $[m, n] = [0, 0]$ component of vorticity, U_{00}, significantly decreases during the ELM suppression phase. Fig.4.14 shows the U_{00} profile for $I_{\mathrm{RMP}} = 0$ kA (ELMy), 2 kA (mitigation), and 4 kA (suppression) cases. Here, U_{00} of the pedestal region decreases when I_{RMP} increases to 2 kA, but it is not much different from the ELMy case. For $I_{\mathrm{RMP}} = 4$ kA, U_{00} is largely degraded. Because U_{00} largely decreases when PBM is included, it suggests that mode coupling suppresses the U_{00} profile. The previous study [103] reported that the perturbed energy of PBM tends to be evenly distributed over n as U_{00} decreases. This finding is consistent with

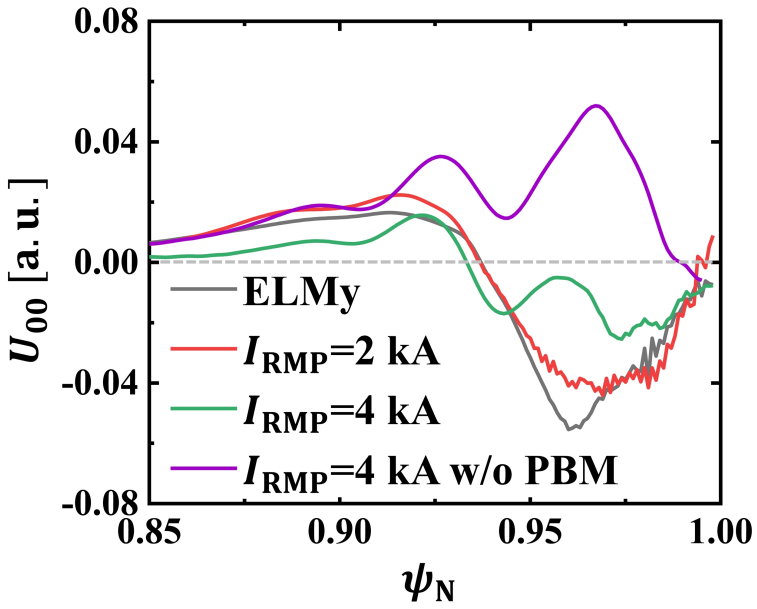

Figure 4.14: The radial profile of plasma vorticity of $[m, n] = [0, 0]$ component is presented for I_{RMP} 0, 2, 4 kA with PBM, and without PBM cases. The dotted gray line represents $U_{00} = 0$.

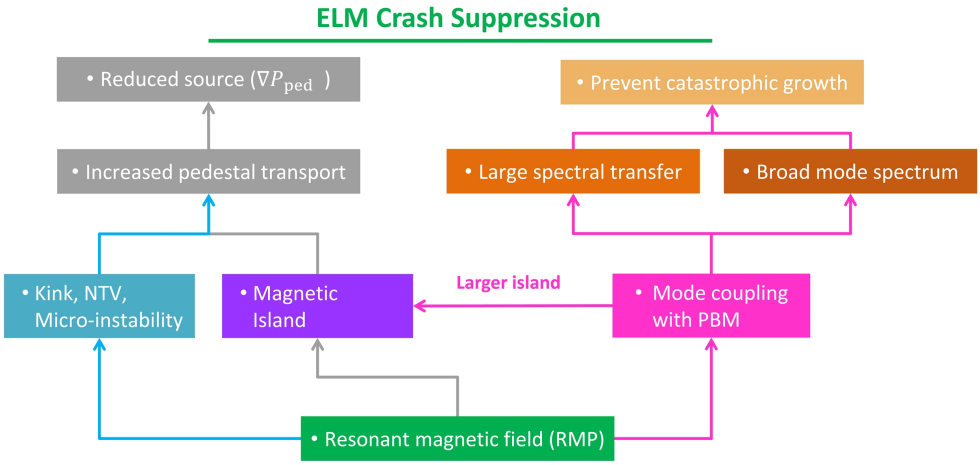

Figure 4.15: The schematic diagram of the correlation between RMP and the ELM crash suppression.

Fig.4.5(d) where the n spectrum of PBM broadens with ELM suppression. The experimental observation [24] also found a similar trend where a single coherent wave transitions to the broadband waves.

When the energy transfer between modes increases and the energies of PBM are evenly distributed to harmonics, a single-mode cannot grow too large to crash. Therefore, RMP acts to increase the coupling between different mode numbers of PBM and results in states with saturated or suppressed modes. This finding is consistent with the previous numerical study that the bursty mode crash disappears when mode couplings between PBMs are reinforced [104]. Overall, the correlation between RMP and ELM crash suppression can be extended as Fig.4.15. In the figure, the conventional and the extended correlations are colored in gray and pink, respectively. From this modeling, one might expect that the plasma condition that can maximize the mode coupling effect is favorable to the ELM suppression. After further investigation, it is confirmed that PBM locking is such a condition.

4.4 RMP-driven PBM locking

A large change is found in the rotation of the mode when ELM suppression is achieved in the simulation. Fig.4.16(a) presents the poloidal rotation of the most unstable mode ($n > 2$) for different RMP coil currents. Here, $V_{\theta,\mathrm{mode}}$ is the poloidal rotation at the midplane of LFS, derived from the simulation in the laboratory frame during the nonlinear phase. In the natural PBM case, a mode shows very oscillatory behavior as the result of nonlinear interaction. The oscillatory behavior of $V_{\theta,\mathrm{mode}}$ decreased overall for $I_{\mathrm{RMP}} = 2$ kA. For $I_{\mathrm{RMP}} = 4$ kA, modes are initially rotating, but start to slow down until they stop rotating at $t \sim 3400\tau_{\mathrm{A}}$. They remain nearly static. Unlike $V_{\theta,\mathrm{mode}}$, the poloidal $E \times B$ rotation $V_{\theta,\mathrm{E}}$ continues to increase. Although it is not shown here, $V_{\theta,\mathrm{E}}$ at the center of the pedestal ($\psi_{\mathrm{N}} = 0.98$) changes from -3 km/s to -10 km/s in the ion-diamagnetic direction as I_{RMP} increases from 0 kA to 4 kA. It shows that RMP brakes PBMs and this is a prominent feature that distinguishes ELM suppression from mitigation.

The sudden braking of ELM after a transition from mitigation to suppression was also observed in the experiments [24, 25]. These experimental results may indicate that the ELM suppression regime consists of static saturated PBMs, while natural or mitigated regimes consist of rotating PBMs. Unfortunately, the mechanism of the mode braking is unclear. The previous numerical study [92] tried to explain the mode braking with the RMP-induced electromagnetic torque [44]. The reduction of perpendicular electron flow is also observed in our modeling, which is consistent with this study. Furthermore, the recent theoretical study proved that nonlinear dynamic plays are important for the locking of the magnetic island and other modes under the presence of RMP [105]. However, there is no direct evidence and quantitative explanations

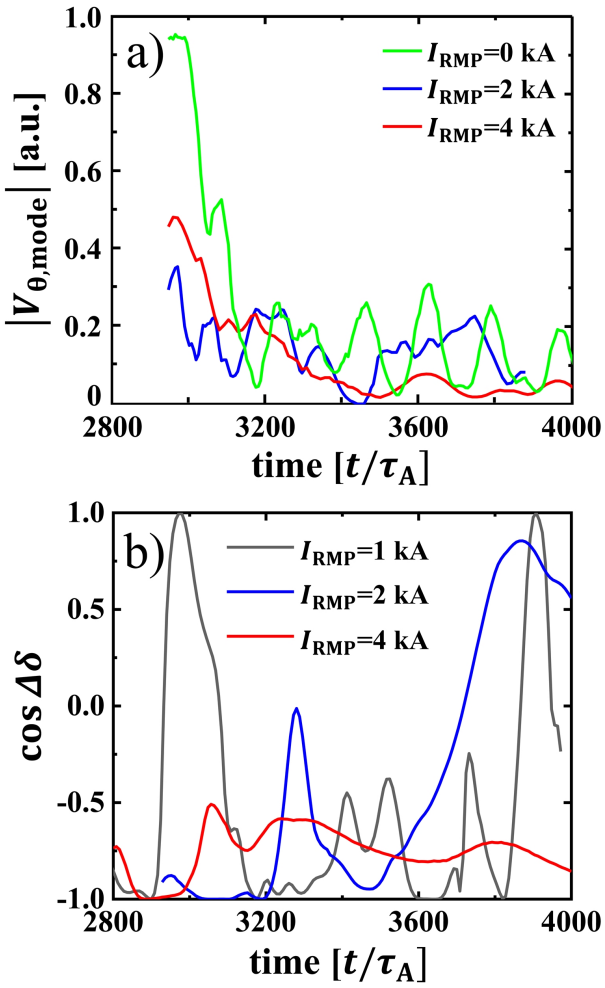

Figure 4.16: a) Time evolution of the poloidal mode rotation $V_{\theta,\mathrm{mode}}$ during the nonlinear phase. It shows $V_{\theta,\mathrm{mode}}$ of the natural PBM ($n = 12$, green line), PBM with $I_{\mathrm{RMP}} = 2$ kA ($n = 6$, blue line), and $I_{\mathrm{RMP}} = 4$ kA ($n = 4$, red line). (b) Time evolution of $\cos\Delta\delta$, where $\Delta\delta$ is the phase difference between $n = 2$ RMP-induced mode and the most unstable harmonic component of PBM for I_{RMP} of 1 kA ($n = 6$, gray line), 2 kA ($n = 6$, blue line), and 4 kA ($n = 4$, red line).

for mode braking with RMP-induced torque yet. Another possible candidate is the interaction between the mode and the magnetic island. In Fig.4.8(a), the magnetic island and $\delta B_{\mathrm{r,even}}$ rapidly increase at $I_{\mathrm{RMP}} \sim 4$ kA, where the mode-locking occurs. The rapid increase in $\delta B_{\mathrm{r,even}}$ implies a strong coupling between PBMs and the magnetic island, so the perturbed field and the coupling effect may have influenced the suppression of mode rotation. Besides, the interaction of the resonant currents with the external fields can also be important because it affects the torque balance with RMP. Further analysis is needed as future work.

4.4.1 Enhanced mode coupling by PBM locking

To understand the role of mode braking in the ELM suppression, we investigate the effect of $V_{\theta,\mathrm{mode}}$ to the mode coupling and ELM suppression for the first time. In our modeling, perturbed quantities X_{n} of a single harmonic is described as

$$X_{\mathrm{n}}(R, Z, \phi) = X_{\mathrm{n}}(R, Z) \cos\left[n\phi + \delta_{\mathrm{n}}(R, Z)\right]. \tag{4.4}$$

In Eq.4.4, $X_{\mathrm{n}}(R, Z)$ and the cosine term catch the poloidal and the toroidal variations of mode, respectively. The mode coupling is affected by their relative spatial position and it is related to the relative phase difference, $\Delta\delta (= \delta_{n1} - \delta_{n2})$.

In the previous section, we concluded that the suppression of PBM may result from energy exchange between $n = 2$ RMP-induced mode and PBMs ($n > 2$). Steady energy transfer between modes is vital in this respect. However, energy transfer will be suppressed if $\Delta\delta$ keeps changing. For example, when we consider the momentum equation, nonlinear terms in $\partial_t u_{\mathrm{n}}$ depends on $\cos\left[\delta_{n1} - \delta_{n2}\right]$, where $n = n_1 - n_2$. Because $\partial_t W_{\mathrm{kin}}$ for n is proportional to

$u_{\rm n}\partial_t u_{\rm n}$, it is also affected by $\Delta\delta$. In addition, the time scale of $\Delta\delta$ is $\sim 100\tau_{\rm A}$ comparable to that of mode fluctuations. Therefore, $\Delta\delta$ should remain constant to maintain consistent energy exchange between modes. It is equivalent to keeping the spatial overlapping of mode structures.

Because the RMP-induced $n = 2$ mode is static in space, $\Delta\delta$ only depends on $V_{\theta,\rm mode}$ of PBM. To keep $\Delta\delta$ constant, $V_{\theta,\rm mode}$ needs to be very small, and mode locking can be advantageous to ELM suppression. In Fig.4.16(b), the phase difference ($\Delta\delta$) between $n = 2$ (RMP) and the largest harmonic of PBM at the mid-plane of LFS is presented. During the nonlinear phase, it clearly shows how $V_{\theta,\rm mode}$ affects $\Delta\delta$. When $I_{\rm RMP} = 1$ kA or 2 kA, $\Delta\delta$ shows considerable variation because of the oscillatory $V_{\theta,\rm mode}$ as shown in Fig.4.16(a). For $I_{\rm RMP} = 4$ kA (ELM suppression case), however, $\cos\Delta\delta$ remains almost constant (~ -0.8) with locking of PBM. Therefore, it can be addressed that PBM locking is the favorable condition which amplifies the coupling of RMP and PBM, resulting in mode suppression.

In the nonlinear phase, $V_{\theta,\rm mode}$ can be expressed as

$$V_{\theta,\rm mode} \approx V_{\theta,\rm E} + V_{\theta,\rm NL}, \tag{4.5}$$

where $V_{\theta,\rm NL}$ is the poloidal mode rotation generated by nonlinear interactions including RMP. We note that when $V_{\theta,\rm E}$ increases, larger $I_{\rm RMP}$ can be needed to drive $V_{\theta,\rm NL}$ to make $V_{\theta,\rm mode}$ vanish. Locking PBMs with RMP becomes more difficult with larger $V_{\theta,\rm E}$. In this context, large $V_{\theta,\rm E}$ will be disadvantageous to ELM suppression.

To test the above hypothesis, the effect of RMP on PBMs with increased $V_{\theta,\rm E}$ is investigated. In this simulation, the $n = 0$ component of $V_{\theta,\rm E}$ at the center of the pedestal is increased from -3 km/s to -15 km/s while other condi-

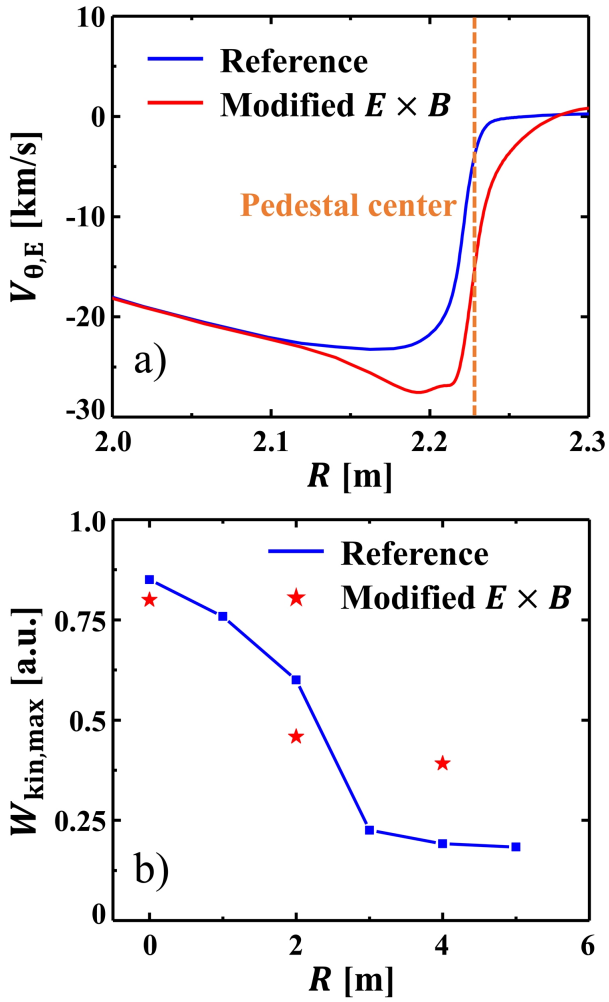

Figure 4.17: a) Radial profile of $E \times B$ poloidal rotation profile at the mid-plane of LFS. Profile of reference case (blue line) and modified case (red line) are presented. Here, the orange dotted line corresponds to the position of the pedestal center, and ion-diamagnetic flow is in (the negative) direction. (b) The largest kinetic energy of PBM during the nonlinear phase for various I_{RMP}. The blue dotted line and red stars correspond to the reference and modified cases, respectively.

tions are fixed. The modified radial profile of $V_{\theta,\mathrm{E}}$ at the edge region is shown in Fig.4.17(a). $W_{\mathrm{kin,max}}$ of PBM in the nonlinear phase with corresponding I_{RMP} is presented in Fig.4.17(b). For the case of modified $V_{\theta,\mathrm{E}}$, the modes are mitigated by RMP similarly to the reference case. However, at $I_{\mathrm{RMP}} = 4$ kA, the suppression of the mode is not achieved and locking of PBM does not occur either. While the pressure gradient at the center of pedestal decreases by 35%, it decreases by 28% in the case with the modified $V_{\theta,\mathrm{E}}$ profile. When $V_{\theta,\mathrm{E}}$ is modified, the $V_{\perp,\mathrm{e}} = 0$ layer is pushed outward from $\psi_{\mathrm{N}} = 0.95$ to 0.97, and the radial width of the stochastic layer is reduced. Thus, the degradation of the pedestal is relatively small. Our results showed that mode coupling plays a more critical role in ELM suppression than the reduction of the pedestal gradient. Therefore, the locking of PBM ($V_{\theta,\mathrm{mode}} \to 0$) is the main factor for the ELM suppression. Furthermore, small $V_{\theta,\mathrm{E}}(\approx 0)$ in the pedestal region will be advantageous in terms of PBM locking. It might be related to the importance of $V_{\theta,\mathrm{E}} \approx 0$ in ELM suppression in experiments [89].

In summary, the favorable conditions for the ELM suppression by RMP can be addressed from our results. They are summarized as Table.4.1, where q_{ped} is q at the pedestal top, M is arbitrary integer value and V_{PBM} is $V_{\theta,\mathrm{mode}}$ of PBM during its linear phase. The mode interaction between RMP and PBM is expected to be amplified under these conditions.

Table 4.1: Favorable conditions for the RMP-driven ELM suppression

Conditions	Purposes
Odd parity coil	- Large kink-peeling response
$q_{\mathrm{ped}} \sim M/n_{\mathrm{RMP}}$	- Island formation near the inner pedestal top
$S_{(\mathrm{M,M+1})} > 1$	- Island overlap to cover the pedestal
$V_{\mathrm{PBM}} \sim 0$	- Advantageous to the PBM locking

Chapter 5

Conclusions and future work

The mechanism of RMP-driven pedestal transport and suppression of ELMs has been studied using nonlinear MHD simulations. KPM, tearing response, NTV transport, and mode coupling between RMP and PBM have been investigated by applying the nonlinear MHD code, JOREK, to the KSTAR experiments.

Chapter 2 described the strategy to reconstruct accurate and physically reliable plasma equilibria. High-quality EFIT equilibrium is an essential component of numerically sensitive simulations. However, there are many obstacles to obtain it. In order to solve these kinetic profile problems, various numerical schemes such as outlier filter and function-based fitting to obtain a smooth core profile were developed. Based on the linear PBM theory, a numerical tool was developed to determine the pedestal structure that satisfies the pedestal instability properties observed in the experiment. In addition, a scheme has been developed to improve the uncertainty in the MSE measurement based on the plasma current profile model. By developing these theoretical and nu-

merical tools, a delicate equilibrium was reconstructed for the nonlinear MHD simulation.

First, the effect of RMP-driven MHD transport is investigated on the pedestal. The kink-peeling and tearing response were numerically reproduced under the presence of RMP. The pedestal pressure gradient is reduced, because the radial transport is enhanced due to the formation of the stochastic layer and $E \times B$ convective flow by tearing and KPM component, respectively. This trend is partially consistent with experimental observation. However, discrepancies in the density and rotation were identified. We introduced the NTV effect to improve the numerical results. It reproduced the drop of toroidal rotation but it is still insufficient to account for the degradation of the density pedestal shown in the experiment. This result suggests that new physic, such as turbulence, must be involved to fully explain the pedestal degradation by RMP.

Then, the numerical reproduction of RMP-driven ELM crash suppression is addressed. The simulation results show that such ELM-crash-suppression is attributable not only to the degraded pedestal but also to direct coupling between PBM and RMP-driven plasma response. The coupling between PBM and RMP can 1) enhance the size of the island across the pedestal, reducing the instability source by further pedestal degradation. It 2) increases the spectral transfer between edge harmonics preventing catastrophic growth and crash of unstable mode. In addition, the locking (or rotation bifurcation) of PBMs has been numerically simulated during the suppression phase. This mode-locking is a distinguishing feature of the mode suppression as rotating mode structure remains for the natural ELM and mode mitigated case. PBM locking can enhance the interactions between PBMs and RMP. Based on these findings, favorable conditions for RMP-ELM suppression is addressed in terms of mode coupling

between RMP and PBM.

These results provide a deeper understanding of pedestal transport and ELM suppression driven by the RMP. However, the analysis is done for a specific KSTAR plasma. It is noteworthy that various RMP and plasma configuration can also contribute to the RMP-driven plasma response. Besides, a more advanced physics model should be included in the simulation to improve the modeling results. Therefore, the further numerical investigation will be needed. The numerical analyses on the $n = 1$ RMP case with accurate transport coefficients, two temperature ($T_i \neq T_e$), n_e continuity equation [80], and extended MHD model are the interesting future works which may extend our understanding of RMP physics.

Bibliography

[1] S. Li *et al. Abstr. Appl. Analysis* **2014**, 1 (2014).

[2] A. Kirk *et al. Phys. Rev. Letters* **96**, 18 (2006).

[3] H. H. Lee *et al.* In *Outer divertor target heat fluxes during resonant magnetic perturbation induced ELM suppressed regimes in KSTAR.* Presented at the 2nd Technical Meeting on Divertor Concepts (IAEA), 13-16 November 2017 in Suzhou, China.

[4] J. W. Connor *et al. Phys. Plasmas* **5**, 7, 2687 (1998).

[5] D. Kim *et al. Plasma Phys. Control. Fusion* **52**, 9, 095009 (2010).

[6] Y. M. Jeon *et al. Phys. Rev. Letters* **109**, 3 (2012).

[7] J. H. Lee *et al. Rev. Sci. Instrum.* **81**, 10, 10D528 (2010).

[8] H. Biglari *et al. Phys. Fluids B* **2**, 1, 1 (1990).

[9] T. S. Hahm *et al. Phys. Plasmas* **2**, 5, 1648 (1995).

[10] C. Challis *et al. Nucl. Fusion* **55**, 5, 053031 (2015).

[11] P. Snyder *et al. Nucl. Fusion* **44**, 2, 320 (2004).

[12] O. Sauter *et al. Phys. Plasmas* **6**, 7, 2834 (1999).

[13] A. Loarte *et al. Plasma Phys. Control. Fusion* **45**, 9, 1549 (2003).

[14] G. Huijsmans *et al. Nucl. Fusion* **53**, 12, 123023 (2013).

[15] L. Baylor *et al. Nucl. Fusion* **49**, 8, 085013 (2009).

[16] J. Rapp *et al. Plasma Phys. Control. Fusion* **44**, 6, 639 (2002).

[17] A. W. Degeling *et al. Plasma Phys. Control. Fusion* **45**, 9, 1637 (2003).

[18] T. E. Evans *et al. Nature Phys.* **2**, 6, 419 (2006).

[19] T. E. Evans *et al. Phys. Rev. Letters* **92**, 23 (2004).

[20] Y. Sun *et al. Phys. Rev. Letters* **117**, 11 (2016).

[21] W. Suttrop *et al. Plasma Phys. Control. Fusion* **59**, 1, 014049 (2016).

[22] R. A. Moyer *et al. Phys. Plasmas* **24**, 10, 102501 (2017).

[23] J.-K. Park *et al. Nature Phys.* **14**, 12, 1223 (2018).

[24] J. Lee *et al. Phys. Rev. Letters* **117**, 7 (2016).

[25] J. Lee *et al. Nucl. Fusion* **59**, 6, 066033 (2019).

[26] L. Lao *et al. Nucl. Fusion* **25**, 11, 1611 (1985).

[27] J. Chung *et al. J. Korean Phys. Society* **65**, 8, 1257 (2014).

[28] W.-H. Ko *et al. Rev. Sci. Instrum.* **81**, 10, 10D740 (2010).

[29] Y. U. Nam *et al. Rev. Sci. Instrum.* **79**, 10, 10E705 (2008).

[30] S.-H. Seo *et al. Rev. Sci. Instrum.* **83**, 10, 10E342 (2012).

[31] M. Newville *et al.* Lmfit: Non-linear least-square minimization and curve-fitting for python (2014).

[32] G. S. Yun *et al. Rev. Sci. Instrum.* **81**, 10, 10D930 (2010).

[33] G. S. Yun *et al. Rev. Sci. Instrum.* **85**, 11, 11D820 (2014).

[34] R. Hager *et al. Phys. Plasmas* **23**, 4, 042503 (2016).

[35] A. Mikhailovskii *et al. Plasma Phys. Rep.* **23**, 10, 844 (1997).

[36] S. Saarelma *et al. Plasma Phys. Control. Fusion* **60**, 1, 014042 (2017).

[37] H. Lütjens *et al. Comput. Phys. Commun.* **97**, 3, 219 (1996).

[38] A. Pankin *et al. Comput. Phys. Commun.* **159**, 3, 157 (2004).

[39] K. Matsuda. *IEEE T. Plasma Sci.* **17**, 1, 6 (1989).

[40] B. W. Rice *et al. Rev. Sci. Instrum.* **70**, 1, 815 (1999).

[41] S. A. Lazerson *et al. Plasma Phys. Control. Fusion* **55**, 8, 084004 (2013).

[42] S. L. and. *Nucl. Fusion* **55**, 2, 023009 (2015).

[43] A. Wingen *et al. Nucl. Fusion* **57**, 1, 016013 (2016).

[44] R. Fitzpatrick. *Phys. Plasmas* **5**, 9, 3325 (1998).

[45] M. Becoulet *et al. Nucl. Fusion* **52**, 5, 054003 (2012).

[46] N. M. Ferraro. *Phys. Plasmas* **19**, 5, 056105 (2012).

[47] N. Ferraro *et al. Nucl. Fusion* **53**, 7, 073042 (2013).

[48] C. Paz-Soldan *et al. Phys. Rev. Letters* **114**, 10 (2015).

[49] F. Orain *et al. Nucl. Fusion* **57**, 2, 022013 (2016).

[50] G. Huysmans *et al. Plasma Phys. Control. Fusion* **51**, 12, 124012 (2009).

[51] M. Bécoulet *et al. Nucl. Fusion* **48**, 2, 024003 (2008).

[52] F. Orain *et al. Phys. Plasmas* **20**, 10, 102510 (2013).

[53] T. A. Gianakon *et al. Phys. Plasmas* **9**, 2, 536 (2002).

[54] C. Kessel. *Nucl. Fusion* **34**, 9, 1221 (1994).

[55] M. Bécoulet *et al. Nucl. Fusion* **57**, 11, 116059 (2017).

[56] O. Czarny *et al. J. Comput. Phys.* **227**, 16, 7423 (2008).

[57] C. Chevalier *et al. Parallel Comput.* **34**, 6-8, 318 (2008).

[58] Y. Liu *et al. Plasma Phys. Control. Fusion* **58**, 11, 114005 (2016).

[59] P. Snyder *et al. Nucl. Fusion* **47**, 8, 961 (2007).

[60] R. Moyer *et al. Nucl. Fusion* **52**, 12, 123019 (2012).

[61] D. Shiraki *et al. Phys. Plasmas* **20**, 10, 102503 (2013).

[62] C. Paz-Soldan *et al. Nucl. Fusion* **56**, 5, 056001 (2016).

[63] E. Nardon *et al. Phys. Plasmas* **14**, 9, 092501 (2007).

[64] M. Leconte *et al. Phys. Plasmas* **22**, 8, 082301 (2015).

[65] M. F. Heyn *et al. Nucl. Fusion* **54**, 6, 064005 (2014).

[66] E. Nardon *et al. Nucl. Fusion* **50**, 3, 034002 (2010).

[67] R. Nazikian *et al. Phys. Rev. Letters* **114**, 10 (2015).

[68] S. R. Haskey *et al. Plasma Phys. Control. Fusion* **57**, 2, 025015 (2015).

[69] G. T. A. Huysmans. *Plasma Phys. Control. Fusion* **47**, 12, 2107 (2005).

[70] W. Zhu *et al. Phys. Rev. Letters* **96**, 22 (2006).

[71] J.-K. Park *et al. Phys. Plasmas* **16**, 5, 056115 (2009).

[72] Y. Liu *et al. Nucl. Fusion* **51**, 8, 083002 (2011).

[73] Y. Liu *et al. Nucl. Fusion* **60**, 3, 036018 (2020).

[74] N. C. Logan *et al. Phys. Plasmas* **20**, 12, 122507 (2013).

[75] J.-K. Park *et al. Phys. Plasmas* **24**, 3, 032505 (2017).

[76] M. Willensdorfer *et al. Phys. Rev. Letters* **119**, 8 (2017).

[77] M. L. Mou *et al. Phys. Plasmas* **25**, 8, 082518 (2018).

[78] F. Waelbroeck *et al. Nucl. Fusion* **52**, 7, 074004 (2012).

[79] J. Callen *et al. Nucl. Fusion* **53**, 11, 113015 (2013).

[80] Q. M. Hu *et al. Phys. Plasmas* **26**, 12, 120702 (2019).

[81] T. Rhee *et al. Nucl. Fusion* **55**, 3, 032004 (2015).

[82] A. B. Rechester *et al. Phys. Rev. Letters* **40**, 1, 38 (1978).

[83] G. Park *et al. Phys. Plasmas* **17**, 10, 102503 (2010).

[84] M. Hölzl *et al. J. Phys. Conf. Ser.* **401**, 012010 (2012).

[85] T. M. Bird *et al. Nucl. Fusion* **53**, 1, 013004 (2012).

[86] I. Holod *et al. Nucl. Fusion* **57**, 1, 016005 (2016).

[87] G. Choi *et al. Nucl. Fusion* **58**, 2, 026001 (2017).

[88] R. Hager *et al. Nucl. Fusion* **59**, 12, 126009 (2019).

[89] C. Paz-Soldan *et al. Nucl. Fusion* **59**, 5, 056012 (2019).

[90] Y. Q. Liu *et al. Plasma Phys. Control. Fusion* **54**, 12, 124013 (2012).

[91] M. Bécoulet *et al. Phys. Rev. Letters* **113**, 11 (2014).

[92] F. Orain *et al. Phys. Plasmas* **26**, 4, 042503 (2019).

[93] J. Kim *et al. Nucl. Fusion* **59**, 9, 096019 (2019).

[94] J. A. Morales *et al. Phys. Plasmas* **23**, 4, 042513 (2016).

[95] I. Krebs *et al. Phys. Plasmas* **20**, 8, 082506 (2013).

[96] S. Pamela *et al. Plasma Phys. Control. Fusion* **58**, 1, 014026 (2015).

[97] S. Kim *et al. Nucl. Fusion* **60**, 2, 026009 (2020).

[98] T. Evans *et al. J. Nucl. Mater.* **337-339**, 691 (2005).

[99] M. Jakubowski *et al. Nucl. Fusion* **49**, 9, 095013 (2009).

[100] A. Thornton *et al. Nucl. Fusion* **54**, 6, 064011 (2014).

[101] Y. In *et al. Nucl. Fusion* **57**, 11, 116054 (2017).

[102] J.-W. Ahn *et al. Nucl. Fusion* **54**, 12, 122004 (2014).

[103] H. Jhang *et al. Nucl. Fusion* **57**, 2, 022006 (2016).

[104] P. Xi *et al. Phys. Rev. Letters* **112**, 8 (2014).

[105] R. Fitzpatrick. *Phys. Plasmas* **27**, 4, 042506 (2020).

초록

플라즈마 경계 불안정성 (ELM) 은 토카막 플라즈마의 경계 페데스탈 영역에서 발생하는 급격한 MHD 불안정성으로, 토카막 내벽과 다이버터에 치명적인 손상을 입힐 수 있다. 따라서, 고성능 플라즈마 운전을 유지하고 핵융합 반응을 일으키기 위해서는 ELM을 억제하는 것이 필수적이다. 과거 실험 연구로부터 공명 자장 섭동 (RMP) 을 통해 ELM 억제가 가능하다는 것이 밝혀졌다. 그러나, RMP를 활용해 ELM을 제어하기 위해서는 특정 조건들이 반드시 충족되어야 하고, 이는 매우 좁은 작동 영역을 갖는다. 그러므로, 안정적인 ELM 제어를 위해서는 RMP-ELM 제어 메커니즘을 이해하는 것이 중요하다.

이 논문은 RMP 인가에 따른 페데스탈 영역의 플라즈마 수송 변화와 ELM 억제 메커니즘에 대한 MHD 기반 수치 연구를 다룬다. 첫째로, KSTAR 플라즈마 대상으로 비선형 MHD 시뮬레이션을 수행하는 데 필요한 고성능 플라즈마 구축 방법론을 개발하였다. 해당 평형 계산의 어려움을 해결하기 위해 이론적 모델과 여러 수치 기법들이 사용되며, 비선형 MHD 연구에 적합한 완성도 높은 플라즈마 평형이 도출되었다.

둘째로, RMP인가에 따른 MHD 기반의 페데스탈 수송 현상을 분석하였다. RMP에 의해 구동되는 뒤틀림-껍질 응답 (KPM) 및 확률적 수송 층이 발생한다. 해당 요소들로 인해 페데스탈 영역에서 대류, 전도성 및 신고전 (NTV) 플라즈마 수송을 증가하며 온도와 밀도 페데스탈의 기울기가 줄어드는 것을 설명하였다. KSTAR 실험에서 관측된 결과와의 비교를 통해 본 MHD 기반의 수송 연구 결과의 타당성을 일부분 확보하였으나, 실험 결과를 완전히 설명하기 위해서는 난류 수송과 같은 추가적인 물리 기작이 필요하다는 것이 확인되었다.

마지막으로, KSTAR 실험과 유사한 조건의 RMP 인가에 따른 ELM 억제 현상을 시뮬레이션 상에서 성공적으로 재현하였다. 이로부터 ELM 억제는 RMP에 의한 페데스탈 기울기의 감소뿐만 아니라 ELM과 RMP 간의 직접적인 상호작용

에 기인하는 것을 밝혀냈다. 이때 상호작용의 효과는 1) 페데스탈 영역의 자장 섬 크기를 증가시켜 추가적인 페데스탈 기울기와 불안정성 발생 요소를 줄이고 2) ELM의 급격한 증가와 붕괴를 방지하는 불안정성 간의 에너지 이동을 증가시키는 것으로 확인되었다. 이와 같은 효과로 인해 ELM은 비선형적으로 포화 상태에 도달하게 되고 지속해서 억제될 수 있다. 추가로 본 연구는 ELM 억제를 위해 해당 RMP-ELM 간의 상호작용을 강화하는 플라즈마 조건을 논의하였다.

주요어: 토카막, 3D 자기장, 경계 페데스탈, 경계 불안정성 제어, KSTAR, PBM, 비선형 MHD

학번: 2014-22715